Physical limitations on antennas of arbitrary shape

Gustafsson, Mats; Sohl, Christian; Kristensson, Gerhard

2007

CODEN:LUTEDX/(TEAT-7153)/1-36/(2007)

Physical limitations on antennas of arbitrary shape

Mats Gustafsson, Christian Sohl, and Gerhard Kristensson

Electromagnetic Theory
Department of Electrical and Information Technology
Lund University
Sweden

Mats Gustafsson, Christian Sohl, and Gerhard Kristensson
{Mats.Gustafsson,Christian.Sohl,Gerhard.Kristensson}@es.lth.se

Department of Electrical and Information Technology
Electromagnetic Theory
P.O. Box 118
SE-221 00 Lund
Sweden

Editor: Gerhard Kristensson

Abstract

In this paper, physical limitations on bandwidth, realized gain, Q-factor, and directivity are derived for antennas of arbitrary shape. The product of bandwidth and realizable gain is shown to be bounded from above by the eigenvalues of the long wavelength high-contrast polarizability dyadics. These dyadics are proportional to the antenna volume and easily determined for an arbitrary geometry. Ellipsoidal antenna volumes are analyzed in detail and numerical results for some generic geometries are presented. The theory is verified against the classical Chu limitations for spherical geometries, and shown to yield sharper bounds for the ratio of the directivity and the Q-factor for non-spherical geometries.

1 Introduction

The concept of physical limitations for electrically small antennas was first introduced more than half a century ago in Refs. 3 and 24, respectively. Since then, much attention has been drawn to the subject and numerous papers have been published, see Ref. 12 and references therein. Unfortunately, almost all these papers are restricted to the sphere via the spherical vector wave expansions, deviating only slightly from the pioneering ideas introduced in Ref. 3.

The objective of this paper is to derive physical limitations on bandwidth, realized gain, Q-factor, and directivity for antennas of arbitrary shape. The limitations presented here generalize in many aspects the classical results by Chu. The most important advantage of the new limitations is that they no longer are restricted to the sphere but instead hold for arbitrary antenna volumes. In fact, the smallest circumscribing sphere is far from optimal for many antennas, *cf.*, the dipole and loop antennas in Sec. 8. Furthermore, the new limitations successfully separate the electric and magnetic material properties of the antennas and quantify them in terms of their polarizability dyadics.

The new limitations introduced here are also important from a radio system point of view. Specifically, they are based on the bandwidth and realizable gain as well as the Q-factor and the directivity. The interpretation of the Q-factor in terms of the bandwidth is still subject to some research, see Ref. 25. Moreover, the new limitations permit the study of polarization effects and their influence on the antenna performance. An example of such an effect is polarization diversity for applications in MIMO communication systems.

The present paper is a direct application of the physical limitations for broadband scattering introduced in Refs. 19 and 20, where the integrated extinction is related to the long wavelength polarizability dyadics. The underlying mathematical description is strongly influenced by the consequences of causality and the summation rules and dispersion relations in the scattering theory for the Schrödinger equation, see Refs. 16, 17 and 22.

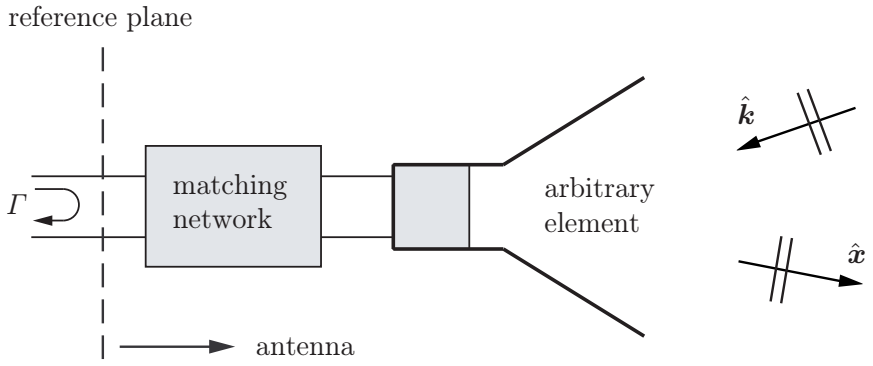

Figure 1: Illustration of a hypothetic antenna subject to an incident plane-wave in the $\hat{\boldsymbol{k}}$-direction.

2 Scattering and absorption of antennas

The present theory is inspired by the general scattering formalism of particles and waves in Refs. 16 and 22. In fact, based on the assumptions of linearity, time-translational invariance and causality there is no fundamental difference between antennas and properly modeled scatterers. This kind of fruitful equivalence between antenna and scattering theory has already been encountered in the literature, *cf.*, the limitations on the absorption efficiency in Ref. 2 and its relation to minimum scattering antennas. Without loss of generality, the integrated extinction and the theory introduced in Ref. 19 can therefore be argued to also hold for antennas of arbitrary shape. In contrast to Ref. 19, the present paper focuses on the absorption cross section rather than scattering properties.

For this purpose, consider an antenna of arbitrary shape surrounded by free space and subject to a plane-wave excitation impinging in the $\hat{\boldsymbol{k}}$-direction, see Fig. 1. The antenna is assumed to be lossless with respect to ohmic losses and satisfy the fundamental principles of linearity, time-translational invariance and causality. The dynamics of the antenna is modeled by the Maxwell equations with general reciprocal anisotropic constitutive relations. The constitutive relations are expressed in terms of the electric and magnetic susceptibility dyadics, $\boldsymbol{\chi}_{\mathrm{e}}$ and $\boldsymbol{\chi}_{\mathrm{m}}$, respectively, which are functions of the material properties of the antenna.

The assumption of a lossless antenna is not severe since the analysis can be modified to include ohmic losses, see the discussion in Sec. 9. In fact, ohmic losses are important for small antennas, and taking such effects into account, suggest that the lossless antenna is more advantageous than the corresponding antenna with ohmic losses. Recall that $\boldsymbol{\chi}_{\mathrm{e}}$ and $\boldsymbol{\chi}_{\mathrm{m}}$ also depend on the angular frequency ω of the incident plane-wave in the presence of losses.

The bounding volume V of the antenna is of arbitrary shape with the restriction that the complete absorption of the incident wave is contained within V. The bounding volume is naturally delimited by a reference plane or a port at which a unique voltage and current relation can be defined, see Fig. 1. The present definition of the antenna structure includes the matching network and is of the same kind as

the descriptions in Refs. 3 and 25. The reflection coefficient Γ at the port is due to the unavoidable impedance mismatch of the antenna over a given wavelength interval, see Ref. 5. The present analysis is restricted to single port antennas with a scalar (single) reflection coefficient. The extension to multiple ports is commented briefly in Sec. 9.

For any antenna, the scattered electric field $\boldsymbol{E}_{\mathrm{s}}$ in the forward direction $\hat{\boldsymbol{k}}$ can be expressed in terms of the forward scattering dyadic $\mathbf{S}$ as, see Appendix A,

$$\boldsymbol{E}_{\mathrm{s}}(k, x\hat{\boldsymbol{k}}) = \frac{\mathrm{e}^{\mathrm{i}kx}}{x}\mathbf{S}(k, \hat{\boldsymbol{k}}) \cdot \boldsymbol{E}_0 + \mathcal{O}(x^{-2}) \quad \text{as } x \to \infty. \tag{2.1}$$

Here, $\boldsymbol{E}_0$ denotes the Fourier amplitude of the incident field $\boldsymbol{E}_{\mathrm{i}}(\mathrm{c}_0 t - \hat{\boldsymbol{k}} \cdot \boldsymbol{x})$, and k is a complex variable with $\operatorname{Re} k = \omega/\mathrm{c}_0$ and $\operatorname{Im} k \geq 0$. For a large class of antennas, the elements of $\mathbf{S}$ are holomorphic in k and Cauchy's integral theorem can be applied to

$$\varrho(k) = \frac{1}{k^2}\hat{\boldsymbol{p}}_{\mathrm{e}}^* \cdot \mathbf{S}(k, \hat{\boldsymbol{k}}) \cdot \hat{\boldsymbol{p}}_{\mathrm{e}}, \quad k \in \mathbb{C}. \tag{2.2}$$

Here, $\hat{\boldsymbol{p}}_{\mathrm{e}} = \boldsymbol{E}_0/|\boldsymbol{E}_0|$ denotes the electric polarization, which is assumed to be independent of k.[1] The complex-valued function (2.2) is referred to as the extinction volume and it provides a holomorphic extension of the extinction cross section to $\operatorname{Im} k \geq 0$, see Appendix A.

A dispersion relation or summation rule for the extinction cross section can be derived in terms of the electric and magnetic polarizability dyadics $\boldsymbol{\gamma}_{\mathrm{e}}$ and $\boldsymbol{\gamma}_{\mathrm{m}}$, respectively. The derivation is based on energy conservation via the optical theorem in Refs. 16 and 22. The optical theorem $\sigma_{\mathrm{ext}} = 4\pi k \operatorname{Im} \varrho$ and the asymptotic behavior of the extinction volume ϱ in the long wavelength limit, $|k| \to 0$, are the key building blocks in the derivation. The result is the integrated extinction

$$\int_0^\infty \sigma_{\mathrm{ext}}(\lambda)\ \mathrm{d}\lambda = \pi^2(\hat{\boldsymbol{p}}_{\mathrm{e}}^* \cdot \boldsymbol{\gamma}_{\mathrm{e}} \cdot \hat{\boldsymbol{p}}_{\mathrm{e}} + \hat{\boldsymbol{p}}_{\mathrm{m}}^* \cdot \boldsymbol{\gamma}_{\mathrm{m}} \cdot \hat{\boldsymbol{p}}_{\mathrm{m}}), \tag{2.3}$$

where the magnetic (or cross) polarization $\hat{\boldsymbol{p}}_{\mathrm{m}} = \hat{\boldsymbol{k}} \times \hat{\boldsymbol{p}}_{\mathrm{e}}$ has been introduced. The functional dependence on $\hat{\boldsymbol{k}}$ and $\hat{\boldsymbol{p}}_{\mathrm{e}}$ is for simplicity suppressed from the argument on the left hand side of (2.3). Note that (2.3) also can be formulated in $k = 2\pi/\lambda$ via the transformation $\sigma_{\mathrm{ext}}(\lambda) \to 2\pi\sigma_{\mathrm{ext}}(2\pi/k)/k^2$. For details on the derivation of (2.3) and definition of the extinction cross section σ_{ext} and the polarizability dyadics $\boldsymbol{\gamma}_{\mathrm{e}}$ and $\boldsymbol{\gamma}_{\mathrm{m}}$, see Appendix A and B. The integrated extinction applied to scattering problems is exploited in Ref. 19.

It is already at this point important to notice that the right hand side of (2.3) only depends on the long wavelength limit or static response of the antenna, while the left hand side is a dynamic quantity which includes the absorption and scattering properties of the antenna. Furthermore, electric and magnetic properties are seen to be treated on equal footing in (2.3), both in terms of material properties and polarization description.

[1] Observe that the assumption that $\hat{\boldsymbol{p}}_{\mathrm{e}}$ is independent of k does not imply that the polarization of the antenna in Fig. 1 is frequency independent.

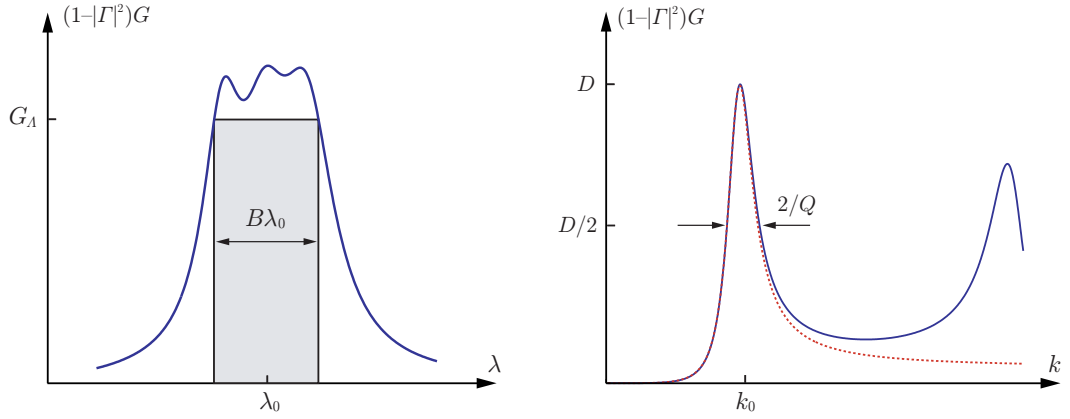

Figure 2: Illustration of the two types of physical limitations considered in this paper: $G_\Lambda B$ represented by the shaded box (left figure) and D/Q related to the dotted resonance model (right figure).

The antenna parameters of importance in this paper are the partial gain G and the partial directivity D, see Appendix E and Ref. 13. In general, both G and D depend on the incident direction $\hat{\boldsymbol{k}}$ and the electric polarization $\hat{\boldsymbol{p}}_{\rm e}$ as well as the wave number k. In addition, the partial realized gain, $(1-|\Gamma|^2)G$, depends on the reflection coefficient Γ. In the forthcoming analysis, the relative bandwidth B, the Q-factor, and the associated center wavelength λ_0 are naturally introduced as intrinsic parameters in the sense that neither of them depend on $\hat{\boldsymbol{k}}$ or $\hat{\boldsymbol{p}}_{\rm e}$ for a given single port antenna.

Two different types of bounds on the first resonance of an antenna are addressed in this paper, see Fig. 2. The bounds relate the integral (2.3) of two generic integrands to the polarizability dyadics. The bound on the partial realized gain, $(1-|\Gamma|^2)G$, in the left figure takes the form of a box, *i.e.*, it estimates the integral with the bandwidth times the partial realized gain. The bound in the right figure utilizes the classical resonance shape of the integrand giving a bound expressed in terms of the partial directivity and the associated Q-factor.

3 Limitations on bandwidth and gain

From the definition of the extinction cross section $\sigma_{\rm ext}$ it is clear that it is non-negative and bounded from below by the absorption cross section $\sigma_{\rm a}$. For an unmatched antenna, $\sigma_{\rm a}$ is reduced by the reflection loss $1-|\Gamma|^2$ according to $\sigma_{\rm a} = (1-|\Gamma|^2)\sigma_{\rm a0}$, where $\sigma_{\rm a0}$ denotes the absorption cross section or partial effective area for the corresponding perfectly matched antenna, see Refs. 18 and 13. The absorption cross section $\sigma_{\rm a0}$ is by reciprocity related to the partial antenna directivity D as $D = 4\pi\sigma_{\rm a0}/\lambda^2$, see Ref. 18. Thus, for any wavelength $\lambda \in [0,\infty)$,

$$\sigma_{\rm ext} \geq \sigma_{\rm a} = (1-|\Gamma|^2)\sigma_{\rm a0} = \frac{1}{4\pi}(1-|\Gamma|^2)\lambda^2 D. \tag{3.1}$$

Recall that D depends on the electric polarization $\hat{\boldsymbol{p}}_{\mathrm{e}}$ as well as the incident direction $\hat{\boldsymbol{k}}$. In the present case of no ohmic losses, the partial gain G coincides with the partial directivity D.

Introduce the wavelength interval $\mathit{\Lambda} = [\lambda_1, \lambda_2]$ with center wavelength $\lambda_0 = (\lambda_2 + \lambda_1)/2$ and associated relative bandwidth

$$B = 2\frac{\lambda_2 - \lambda_1}{\lambda_2 + \lambda_1} = 2\frac{k_1 - k_2}{k_2 + k_1},$$

where $0 < B \leq 2$ and $k = 2\pi/\lambda \in K$ denotes the angular wave number in $K = [k_2, k_1]$. Thus, for any wavelength interval $\mathit{\Lambda}$, the estimate $\sigma_{\mathrm{ext}} \geq \sigma_{\mathrm{a}}$ in (3.1) yields

$$\int_0^\infty \sigma_{\mathrm{ext}}(\lambda)\ \mathrm{d}\lambda \geq \int_{\mathit{\Lambda}} \sigma_{\mathrm{a}}(\lambda)\ \mathrm{d}\lambda = \frac{1}{4\pi}\int_{\mathit{\Lambda}} (1 - |\mathit{\Gamma}|^2)\lambda^2 G(\lambda)\ \mathrm{d}\lambda, \tag{3.2}$$

where $D = G$ is used.[2]

In order to simplify the notation, introduce $G_\Lambda = \inf_{\lambda \in \mathit{\Lambda}}(1 - |\mathit{\Gamma}|^2)G$ as the minimum partial realized gain over the wavelength interval $\mathit{\Lambda}$. Following this notation, the integral on the right hand side of (3.2) can be estimated from below as

$$\int_{\mathit{\Lambda}} (1 - |\mathit{\Gamma}|^2)\lambda^2 G(\lambda)\ \mathrm{d}\lambda \geq G_\Lambda \int_{\mathit{\Lambda}} \lambda^2\ \mathrm{d}\lambda = \lambda_0^3 G_\Lambda B\left(1 + \frac{B^2}{12}\right). \tag{3.3}$$

Without loss of generality, the factor $1 + B^2/12$ can be estimated from below by unity. This estimate is also supported by the fact that $B \ll 2$ in many applications. Based upon this observation, (2.3), (3.2) and (3.3) can be summarized to yield the following limitation on the product $G_\Lambda B$ valid for any antenna satisfying the general assumptions stated in Sec. 2:

$$G_\Lambda B \leq \frac{4\pi^3}{\lambda_0^3}(\hat{\boldsymbol{p}}_{\mathrm{e}}^* \cdot \boldsymbol{\gamma}_{\mathrm{e}} \cdot \hat{\boldsymbol{p}}_{\mathrm{e}} + \hat{\boldsymbol{p}}_{\mathrm{m}}^* \cdot \boldsymbol{\gamma}_{\mathrm{m}} \cdot \hat{\boldsymbol{p}}_{\mathrm{m}}). \tag{3.4}$$

Relation (3.4) is one of the main results of this paper. Note that the factor $4\pi^3/\lambda_0^3$ neatly can be expressed as $k_0^3/2$ in terms of the angular wave number $k_0 = 2\pi/\lambda_0$.

The estimate $1 + B^2/12 \geq 1$ in (3.3) is motivated by the simple form of (3.4). In broadband applications, B is in general not small compared to unity, and the higher order term in B should be included on the left hand side of (3.4).

The right hand side of (3.4) depends on both $\hat{\boldsymbol{p}}_{\mathrm{e}}$ and $\hat{\boldsymbol{k}} = \hat{\boldsymbol{p}}_{\mathrm{e}} \times \hat{\boldsymbol{p}}_{\mathrm{m}}$, as well as the long wavelength limit (static limit with respect to $k = 2\pi/\lambda$) material properties and shape of the antenna. It is indeed surprising that it is just the long wavelength limit properties of the antenna that bound the product $G_\Lambda B$ in (3.4). Since $\boldsymbol{\gamma}_{\mathrm{e}}$ and $\boldsymbol{\gamma}_{\mathrm{m}}$ are proportional to the volume V of the antenna, see Ref. 19, it follows from (3.4) that the upper bound on the product $G_\Lambda B$ is directly proportional to V/λ_0^3 or $k_0^3 a^3$, where a denotes the radius of the volume-equivalent sphere.

[2]The equality sign on the left hand side in (3.2) is motivated by the broadband absorption efficiency introduced in (3.7).

In many antenna applications it is desirable to bound the product $G_\Lambda B$ independently of the material properties. For this purpose, introduce the high-contrast polarizability dyadic $\boldsymbol{\gamma}_\infty$ as the limit of either $\boldsymbol{\gamma}_\mathrm{e}$ or $\boldsymbol{\gamma}_\mathrm{m}$ when the elements of $\boldsymbol{\chi}_\mathrm{e}$ or $\boldsymbol{\chi}_\mathrm{m}$ in the long wavelength limit simultaneously approach infinity.[3] Note that this definition implies that $\boldsymbol{\gamma}_\infty$ is independent of any material properties, depending only on the geometry of the antenna. From the variational properties of $\boldsymbol{\gamma}_\mathrm{e}$ and $\boldsymbol{\gamma}_\mathrm{m}$ discussed in Ref. 19 and references therein, it follows that both $\boldsymbol{\gamma}_\mathrm{e}$ and $\boldsymbol{\gamma}_\mathrm{m}$ are bounded from above by $\boldsymbol{\gamma}_\infty$. Hence, (3.4) yields

$$G_\Lambda B \leq \frac{4\pi^3}{\lambda_0^3}(\hat{\boldsymbol{p}}_\mathrm{e}^* \cdot \boldsymbol{\gamma}_\infty \cdot \hat{\boldsymbol{p}}_\mathrm{e} + \hat{\boldsymbol{p}}_\mathrm{m}^* \cdot \boldsymbol{\gamma}_\infty \cdot \hat{\boldsymbol{p}}_\mathrm{m}). \tag{3.5}$$

The introduction of the high-contrast polarizability dyadic $\boldsymbol{\gamma}_\infty$ in (3.5) is the starting point of the analysis below.

The high-contrast polarizability dyadic $\boldsymbol{\gamma}_\infty$ is real-valued and symmetric, and consequently diagonalizable with real-valued eigenvalues. Let $\gamma_1 \geq \gamma_2 \geq \gamma_3$ denote the three eigenvalues. Based on the constraint $\hat{\boldsymbol{p}}_\mathrm{e} \cdot \hat{\boldsymbol{p}}_\mathrm{m} = 0$, which is a consequence of the free space plane-wave excitation, the right hand side of (3.5) can be estimated from above as

$$\sup_{\hat{\boldsymbol{p}}_\mathrm{e} \cdot \hat{\boldsymbol{p}}_\mathrm{m} = 0} G_\Lambda B \leq \frac{4\pi^3}{\lambda_0^3}(\gamma_1 + \gamma_2). \tag{3.6}$$

The interpretation of the operator $\sup_{\hat{\boldsymbol{p}}_\mathrm{e} \cdot \hat{\boldsymbol{p}}_\mathrm{m} = 0}$ is polarization matching, *i.e.*, the polarization of the antenna coincides with the polarization of the incident wave. In the case of non-magnetic antennas, $\boldsymbol{\gamma}_\mathrm{m} = \mathbf{0}$, the second eigenvalue γ_2 in (3.6) vanishes. Hence, the right hand side of (3.6) can be improved by at most a factor of two by utilizing magnetic materials. Note that the upper bounds in (3.5) and (3.6) coincide when $\boldsymbol{\gamma}_\infty$ is isotropic.

Since γ_1 and γ_2 only depend on the long wavelength properties of the antenna, they can easily be calculated for arbitrary geometries using either the finite element method (FEM) or the method of moments (MoM). Numerical results of γ_1 and γ_2 for the Platonic solids, the rectangular parallelepiped and some classical antennas are presented in Secs. 7 and 8. Important variational properties of γ_j are discussed in Ref. 19 and references therein. The influence of supporting ground planes and the validity of the method of images for high-contrast polarizability calculations are presented in Appendix C.

The estimate in (3.2) can be improved based on a priori knowledge of the scattering properties of the antenna. In fact, $\sigma_\mathrm{ext} \geq \sigma_\mathrm{a}$ in (3.1) may be replaced by $\sigma_\mathrm{ext} = \sigma_\mathrm{a}/\eta$, where $0 < \eta \leq 1$ denotes the absorption efficiency of the antenna, see Ref. 2. For most antennas at the resonance frequency, $\eta \leq 1/2$, but exceptions from this rule of thumb exist. In particular, minimum scattering antennas (MSA) defined by $\eta = 1/2$ yield an additional factor of two on the right hand side of (3.1). The inequality in (3.2) can be replaced by the equality

$$\int_\Lambda \sigma_\mathrm{ext}(\lambda)\ \mathrm{d}\lambda = \widetilde{\eta}^{-1} \int_\Lambda \sigma_\mathrm{a}(\lambda)\ \mathrm{d}\lambda. \tag{3.7}$$

[3] Recall that $\boldsymbol{\chi}_\mathrm{e}$ and $\boldsymbol{\chi}_\mathrm{m}$ are real-valued in the long wavelength limit. In the case of finite or infinite conductivity, see Appendix B.

The constant $\widetilde{\eta}$ is bounded from above by the absorption efficiency via $\widetilde{\eta} \leq \sup_{\lambda\in\Lambda} \eta$, and provides a broadband generalization of the absorption efficiency. If $\widetilde{\eta}$ is invoked in (3.2), the right hand side of the inequalities (3.4), (3.5), and (3.6) are sharpened by the multiplicative factor $\widetilde{\eta}$.

4 Limitations on Q-factor and directivity

Under the assumption of N non-interfering resonances characterized by the real-valued angular wave numbers k_n, a multiple resonance model for the absorption cross section is

$$\sigma_{\mathrm{a}}(k) = 2\pi \sum_{n=1}^{N} \varrho_n \frac{Q_n k_n}{1 + Q_n^2 (k/k_n - k_n/k)^2/4}, \tag{4.1}$$

where k is assumed real-valued and ϱ_n are positive weight functions satisfying $\sum_n \varrho_n = \varrho(0)$. Here, the Q-factor of the resonance at k_n is denoted by Q_n, and for $Q_n \gg 1$, the associated relative half-power bandwidth is $B_n \sim 2/Q_n$, see Fig. 3. Recall that $Q_n \geq 1$ is consistent with $0 < B_n \leq 2$. For the resonance model (4.1), one can argue that Q_n in fact coincides with the corresponding antenna Q-factor in Appendix F when the relative bandwidth $2/Q_n$ is based on the half-power threshold, see also Refs. 6 and 25. In the case of strongly interfering resonances, the model (4.1) either has to be modified or the estimates in Sec. 3 have to be used.

The absorption cross section is the imaginary part, $\sigma_{\mathrm{a}} = 4\pi k \operatorname{Im} \varrho_{\mathrm{a}}$, of the function

$$\varrho_{\mathrm{a}}(k) = \sum_{n=1}^{N} \varrho_n \frac{\mathrm{i} Q_n k_n/(2k)}{1 - \mathrm{i} Q_n \left(k/k_n - k_n/k\right)/2}, \tag{4.2}$$

for real-valued k. The function $\varrho_{\mathrm{a}}(k)$ is holomorphic for $\operatorname{Im} k > 0$ and has a symmetrically distributed pair of poles for $\operatorname{Im} k < 0$, see Fig. 3. The integrated absorption cross section is

$$\frac{1}{4\pi^2} \int_{-\infty}^{\infty} \frac{\sigma_{\mathrm{a}}(k)}{k^2} \, \mathrm{d}k = \varrho_{\mathrm{a}}(0) = \widetilde{\eta} \varrho(0) \leq \varrho(0), \tag{4.3}$$

where $\varrho(0)$ is given by the long wavelength limit (A.4).

For antennas with a dominant first resonance at $k = k_1$, it follows from (3.1) and (4.1) that the partial realized gain G satisfies

$$(1 - |\Gamma|^2) G = \frac{k^2 \sigma_{\mathrm{a}}}{\pi} \leq \varrho(0) \frac{2k^2 Q k_1}{1 + Q^2 (k/k_1 - k_1/k)^2/4}, \tag{4.4}$$

where $\varrho_1 \leq \varrho(0)$ has been used. The right hand side of (4.4) reaches its maximum value $\varrho(0) 2k_1^3 Q/(1 - Q^{-2})$ at $k_0 = k_1(1 - 2Q^{-2})^{-1/2}$ or $k_0 = k_1 + \mathcal{O}(Q^{-2})$ as $Q \to \infty$. Hence, k_0 is a good approximation to k_1 if $Q \gg 1$. For a lossless antenna which is perfectly matched at $k = k_0$, the partial realized gain $(1 - |\Gamma|^2)G$ coincides with the partial directivity D. Under this assumption, (4.4) yields $D/Q \leq \varrho(0) 2k_1^3/(1 - Q^{-2})$ which further can be estimated from above as

$$\frac{D}{Q} \leq \frac{k_0^3}{2\pi} \left(\hat{\boldsymbol{p}}_{\mathrm{e}}^* \cdot \boldsymbol{\gamma}_{\mathrm{e}} \cdot \hat{\boldsymbol{p}}_{\mathrm{e}} + \hat{\boldsymbol{p}}_{\mathrm{m}}^* \cdot \boldsymbol{\gamma}_{\mathrm{m}} \cdot \hat{\boldsymbol{p}}_{\mathrm{m}} \right), \tag{4.5}$$

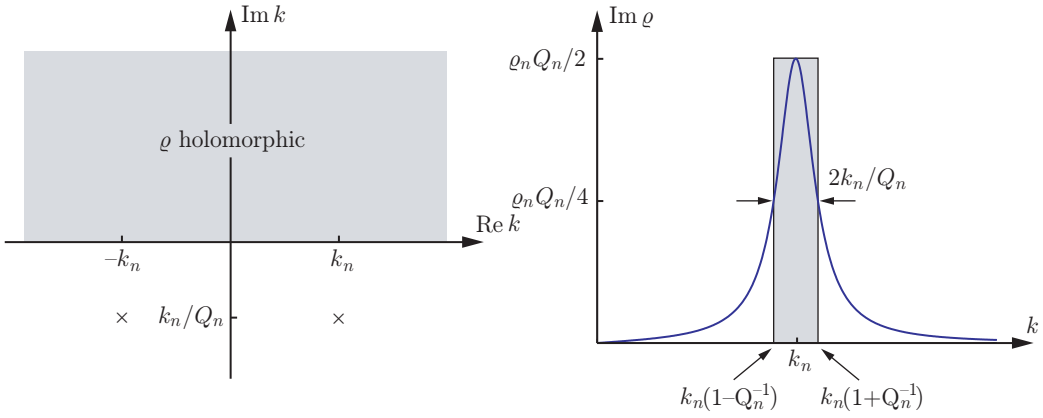

Figure 3: The symmetrically distributed pair of poles (×) of the extinction volume ϱ in the complex k-plane (left figure) and the corresponding single resonance model of $\mathrm{Im}\,\varrho$ when $Q_n \gg 1$ (right figure).

where (A.4) have been used. Relation (4.5) together with (3.5) constitute the main results of this paper.

Analogous to (3.5) and (3.6), it is clear that (4.5) can be estimated from above by the high-contrast polarizability dyadic $\boldsymbol{\gamma}_\infty$ and the associated eigenvalues γ_1 and γ_2, *viz.*,

$$\sup_{\hat{\boldsymbol{p}}_\mathrm{e}\cdot\hat{\boldsymbol{p}}_\mathrm{m}=0} \frac{D}{Q} \leq \frac{k_0^3}{2\pi}(\gamma_1+\gamma_2). \tag{4.6}$$

Here, (4.6) is subject to polarization matching and therefore independent of the electric and magnetic polarizations, $\hat{\boldsymbol{p}}_\mathrm{e}$ and $\hat{\boldsymbol{p}}_\mathrm{m}$, respectively. Note that the upper bounds in (4.5) and (4.6) only differ from the corresponding results in (3.5) and (3.6) by a factor of π, *i.e.*, $G_\Lambda B \leq \pi C$ and $D/Q \leq C$. Hence, it is sufficient to consider either the $G_\Lambda B$ bound or the D/Q bound for a specific antenna. The estimates (4.5) and (4.6) can be improved by the multiplicative factor $\widetilde{\eta}$ if a priori knowledge of the scattering properties of the antenna (3.7) is invoked in (4.4).

The resonance model for the absorption cross section in (4.1) is also directly applicable to the theory of broadband scattering in Ref. 19. In that reference, (4.1) can be used to model absorption and scattering properties and yield new limitations on broadband scattering.

5 Comparison with Chu and Chu-Fano

In this section, the bounds on $G_\Lambda B$ and D/Q subject to matched polarizations, *i.e.*, inequalities (3.6) and (4.6), are compared with the corresponding results by Chu and Fano in Refs. 3 and 5, respectively.

5.1 Limitations on Q-factor and directivity

The classical limitations derived by Chu in Ref. 3 relate the Q-factor and the directivity D to the quantity $k_0 a$ of the smallest circumscribing sphere. Using the notation of Secs. 3 and 4, the classical result by Chu for an omni-directional antenna (for example in the azimuth plane) reads

$$\sup_{\hat{\boldsymbol{p}}_{\rm e}\cdot\hat{\boldsymbol{p}}_{\rm m}=0} \frac{D}{Q} \le \frac{3}{2}\frac{k_0^3 a^3}{k_0^2 a^2+1} = \frac{3}{2}k_0^3 a^3 + \mathcal{O}(k_0^5 a^5) \quad \text{as } k_0 a \to 0. \tag{5.1}$$

In the general case of both TE- and TM-modes, (5.1) must be modified, see Ref. 12, *viz.*,

$$\sup_{\hat{\boldsymbol{p}}_{\rm e}\cdot\hat{\boldsymbol{p}}_{\rm m}=0} \frac{D}{Q} \le \frac{6k_0^3 a^3}{2k_0^2 a^2+1} = 6k_0^3 a^3 + \mathcal{O}(k_0^5 a^5) \quad \text{as } k_0 a \to 0. \tag{5.2}$$

Note that (5.2) differs from (5.1) by approximately a factor of four when $k_0 a \ll 1$.

The bounds in (5.1) and (5.2) should be compared with the corresponding result in Sec. 4 for the sphere. For a sphere of radius a, the eigenvalues γ_1 and γ_2 are degenerated and equal to $4\pi a^3$, see Sec. 6. Insertion of $\gamma_1 = \gamma_2 = 4\pi a^3$ into (4.6) yields $\sup_{\hat{\boldsymbol{p}}_{\rm e}\cdot\hat{\boldsymbol{p}}_{\rm m}=0} D/Q \le C$, where the constant C is given by

$$C = 4k_0^3 a^3, \qquad C = 2k_0^3 a^3, \qquad C = k_0^3 a^3. \tag{5.3}$$

The three different cases in (5.3) correspond to both electric and magnetic material properties ($C = 4k_0^3 a^3$), pure electric material properties ($C = 2k_0^3 a^3$), and pure electric material properties with a priori knowledge of minimum scattering characteristics ($C = k_0^3 a^3$ with $\widetilde{\eta} = 1/2$), respectively. Note that the third case in (5.3) more generally can be expressed as $C = 2k_0^3 a^3 \widetilde{\eta}$ for any broadband absorption efficiency $0 < \widetilde{\eta} \le 1$. The bounds in (5.2) and (5.3) are comparable although the new limitations (5.3) are sharper. In the omni-directional case, (5.1) provides a sharper bound than (5.3), except for the pure electric case with absorption efficiency $\widetilde{\eta} < 3/4$.

5.2 Limitations on bandwidth and gain

The limitation (3.6) should also be compared with the result of Chu when the Fano theory of broadband matching is used. The Fano theory includes the impedance variation over the frequency interval to yield limitations on the bandwidth, see Ref. 5. For a resonance circuit model, the Fano theory yields that the relation between B and Q is, see Ref. 6,

$$B \le \frac{\pi}{Q \ln 1/|\Gamma|}. \tag{5.4}$$

The reflection coefficient Γ is due to mismatch of the antenna. It is related to the standing wave ratio SWR as $|\Gamma| = (\mathrm{SWR}-1)/(1+\mathrm{SWR})$.

Introduce $Q_{\rm s}$ as the Q-factor of the smallest circumscribing sphere with $1/Q_{\rm s} = k_0^3 a^3 + \mathcal{O}(k_0^5 a^5)$ as $k_0 a \to 0$ for omni-directional antennas. Under this assumption, it

follows from (5.1) that $\sup_{\hat{\boldsymbol{p}}_\mathrm{e}\cdot\hat{\boldsymbol{p}}_\mathrm{m}=0} D \leq 3Q/2Q_\mathrm{s}$. Insertion of this inequality into (5.4) then yields

$$\sup_{\hat{\boldsymbol{p}}_\mathrm{e}\cdot\hat{\boldsymbol{p}}_\mathrm{m}=0} G_\Lambda B \leq \frac{3\pi}{2}\frac{1-|\Gamma|^2}{\ln 1/|\Gamma|}k_0^3a^3. \tag{5.5}$$

For a given k_0a, the right hand side of (5.5) is monotone in $|\Gamma|$ and bounded from above by $3\pi k_0^3a^3$. However, note that the Chu-Fano limitation (5.5) is restricted to omni-directional antennas with $k_0a \ll 1$.

Inequality (5.5) should be compared with the corresponding result in Sec. 3 for the smallest circumscribing sphere. Since the upper bounds (3.6) and (4.6) only differ by a factor of π, *i.e.*, $\sup_{\hat{\boldsymbol{p}}_\mathrm{e}\cdot\hat{\boldsymbol{p}}_\mathrm{m}=0} G_\Lambda B \leq C'$ and $\sup_{\hat{\boldsymbol{p}}_\mathrm{e}\cdot\hat{\boldsymbol{p}}_\mathrm{m}=0} D/Q \leq C$ where $C' = \pi C$, it follows from (5.3) that

$$C' = 4\pi k_0^3a^3, \qquad C' = 2\pi k_0^3a^3, \qquad C' = \pi k_0^3a^3. \tag{5.6}$$

The three cases in (5.3) correspond to both electric and magnetic material properties ($C' = 4\pi k_0^3a^3$), pure electric material properties ($C' = 2\pi k_0^3a^3$), and pure electric material properties with a priori knowledge of minimum scattering characteristics ($C' = \pi k_0^3a^3$), respectively.

The limitations on $G_\Lambda B$ based on (5.6) are comparable with (5.5) for most reflections coefficients $|\Gamma|$. For $|\Gamma| < 0.65$ the Chu-Fano limitation (5.5) provides a slightly sharper bound on $G_\Lambda B$ than (5.6) for pure electric materials. However, recall that the spherical geometry gives an unfavorable comparison with the present theory, since for many antennas the eigenvalues γ_1 and γ_2 are reduced considerably compared with the smallest circumscribing sphere, *cf.*, the dipole in Sec. 8.1 and the loop antenna in Sec. 8.2.

6 Ellipsoidal geometries

Closed-form expressions of $\boldsymbol{\gamma}_\mathrm{e}$ and $\boldsymbol{\gamma}_\mathrm{m}$ exist for the ellipsoidal geometries, see Ref. 19, *viz.*,

$$\boldsymbol{\gamma}_\mathrm{e} = V\boldsymbol{\chi}_\mathrm{e}\cdot(\mathbf{I}+\mathbf{L}\cdot\boldsymbol{\chi}_\mathrm{e})^{-1}, \qquad \boldsymbol{\gamma}_\mathrm{m} = V\boldsymbol{\chi}_\mathrm{m}\cdot(\mathbf{I}+\mathbf{L}\cdot\boldsymbol{\chi}_\mathrm{m})^{-1}. \tag{6.1}$$

Here, $\mathbf{I}$ denotes the unit dyadic and $V = 4\pi a_1a_2a_3/3$ is the volume of ellipsoid in terms of the semi-axes a_j. The depolarizability dyadic $\mathbf{L}$ is real-valued and symmetric, and hence diagonalizable with real-valued eigenvalues. The eigenvalues of $\mathbf{L}$ are the depolarizing factors L_j, given by

$$L_j = \frac{a_1a_2a_3}{2}\int_0^\infty \frac{\mathrm{d}s}{(s+a_j^2)\sqrt{(s+a_1^2)(s+a_2^2)(s+a_3^2)}}, \quad j = 1,2,3. \tag{6.2}$$

The depolarizing factors L_j satisfy $0 \leq L_j \leq 1$ and $\sum_j L_j = 1$. The semi-axes a_j are assumed to be ordered such that $L_1 \leq L_2 \leq L_3$. Closed-form expressions of (6.2) in terms of the semi-axis ratio $\xi = (\min_j a_j)/(\max_j a_j)$ exist for the ellipsoids of revolution, *i.e.*, the prolate spheroids ($L_2 = L_3$) and the oblate spheroids ($L_1 = L_2$), see Appendix G.

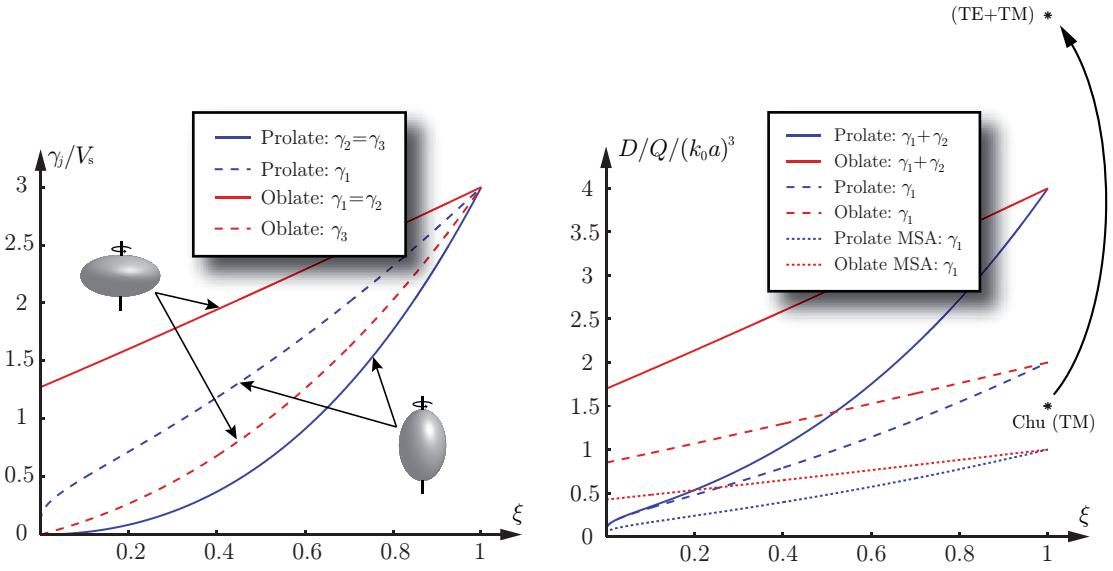

Figure 4: The eigenvalues $\gamma_1 \geq \gamma_2 \geq \gamma_3$ (left figure) and the quotient D/Q (right figure) for the prolate and oblate spheroids as function of the semi-axis ratio ξ. Note the normalization with the volume $V_s = 4\pi a^3/3$ of the smallest circumscribing sphere.

The high-contrast polarizability dyadic $\boldsymbol{\gamma}_\infty$ is given by (6.1) as the elements of $\boldsymbol{\chi}_e$ or $\boldsymbol{\chi}_m$ simultaneously approach infinity. From (6.1) it is clear that the eigenvalues of $\boldsymbol{\gamma}_\infty$ are given by $\gamma_j = V/L_j$. For the prolate and oblate spheroids, V is neatly expressed in terms of the volume $V_s = 4\pi a^3/3$ of the smallest circumscribing sphere. The results are $V = \xi^2 V_s$ and $V = \xi V_s$ for the prolate and oblate spheroids, respectively. The eigenvalues γ_1 and γ_2 for the prolate and oblate spheroids are depicted in the left figure in Fig. 4. Note that the curves for the oblate spheroid approach $4/\pi$ in the limit as $\xi \to 0$, see Appendix G. The corresponding limiting value for the curves as $\xi \to 1$ is 3.

The general bound on $G_\Lambda B$ for arbitrary ellipsoidal geometries is obtained by inserting (6.1) into (3.4), *i.e.*,

$$G_\Lambda B \leq \frac{4\pi^3 V}{\lambda_0^3} \left(\hat{\boldsymbol{p}}_e^* \cdot \boldsymbol{\chi}_e \cdot (\mathbf{I} + \mathbf{L} \cdot \boldsymbol{\chi}_e)^{-1} \cdot \hat{\boldsymbol{p}}_e + \hat{\boldsymbol{p}}_m^* \cdot \boldsymbol{\chi}_m \cdot (\mathbf{I} + \mathbf{L} \cdot \boldsymbol{\chi}_m)^{-1} \cdot \hat{\boldsymbol{p}}_m \right). \quad (6.3)$$

Independent of both material properties and polarization effects, the right hand side of (6.3) can be estimated from above in analogy with (3.6). The result is

$$\sup_{\hat{\boldsymbol{p}}_e \cdot \hat{\boldsymbol{p}}_m = 0} G_\Lambda B \leq \frac{4\pi^3 V}{\lambda_0^3} \left(\frac{1}{L_1} + \frac{1}{L_2} \right). \quad (6.4)$$

In the non-magnetic case, the second term on the right hand side of (6.3) and (6.4) vanishes. For the prolate and oblate spheroids, the closed-form expressions of L_j in Appendix G can be introduced to yield explicit upper bounds on $G_\Lambda B$.

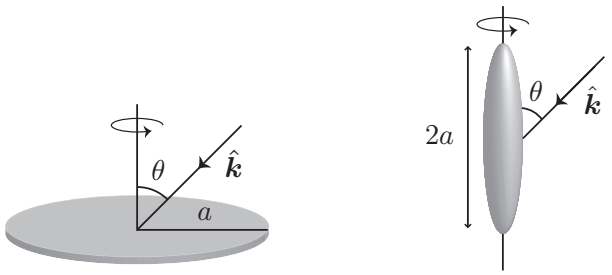

circular disk circular needle

Figure 5: Geometry of the circular disk and needle.

The corresponding results for the quotient D/Q are obtained from the observation that $G_\Lambda B \leq \pi C$ is equivalent to $D/Q \leq C$, see Sec. 4. For the general case including polarization and material properties, (6.3) yields

$$\frac{D}{Q} \leq \frac{k_0^3 V}{2\pi} \left(\hat{\boldsymbol{p}}_{\mathrm{e}}^* \cdot \boldsymbol{\chi}_{\mathrm{e}} \cdot (\mathbf{I} + \mathbf{L} \cdot \boldsymbol{\chi}_{\mathrm{e}})^{-1} \cdot \hat{\boldsymbol{p}}_{\mathrm{e}} + \hat{\boldsymbol{p}}_{\mathrm{m}}^* \cdot \boldsymbol{\chi}_{\mathrm{m}} \cdot (\mathbf{I} + \mathbf{L} \cdot \boldsymbol{\chi}_{\mathrm{m}})^{-1} \cdot \hat{\boldsymbol{p}}_{\mathrm{m}} \right). \tag{6.5}$$

Analogous to (6.4), the restriction to matched polarizations for the quotient D/Q reads

$$\sup_{\hat{\boldsymbol{p}}_{\mathrm{e}} \cdot \hat{\boldsymbol{p}}_{\mathrm{m}} = 0} \frac{D}{Q} \leq \frac{k_0^3 V}{2\pi} \left(\frac{1}{L_1} + \frac{1}{L_2} \right). \tag{6.6}$$

The upper bound in (6.6) is depicted in the right figure in Fig. 4 for the prolate and oblate spheroids. The solid curves correspond to combined electric and magnetic material properties, while the dashed curves represent the pure electric case. The non-magnetic minimum scattering case ($\widetilde{\eta} = 1/2$) is given by the dotted curves. Note that the three curves in the right figure vanish for the prolate spheroid as $\xi \to 0$. The corresponding limiting values for the oblate spheroid are $16/3\pi$, $8/3\pi$ and $4/3\pi$, see Appendix G.

The curves depicted in the right figure in Fig. 4 should be compared with the classical results for the sphere in (5.1) and (5.2). The omni-directional bound (5.1) and its generalization (5.2) are marked in Fig. 4 by Chu (TE) and (TE+TM), respectively. From the figure, it is clear that (6.6) provides a sharper bound than (5.2). For omni-directional antennas, (5.1) is slightly sharper than (6.6) for the sphere, but when a priori knowledge of minimum scattering characteristics ($\widetilde{\eta} = 1/2$) is used, the reversed conclusion holds. Recall that the classical results in Sec. 5.1 are restricted to the sphere, in contrast to the theory introduced in this paper.

Based on the results in Appendix G, it is interesting to evaluate (6.4) in the limit as $\xi \to 0$. This limit corresponds to the axially symmetric needle and circular disk in Fig. 5. For a needle of length $2a$ with semi-axis $\xi \ll 1$, (G.3) inserted into (6.4) yields

$$G_\Lambda B \leq \frac{16\pi^4 a^3}{3\lambda_0^3} \frac{f(\theta)}{\ln 2/\xi - 1} + \mathcal{O}(\xi^2) \quad \text{as } \xi \to 0. \tag{6.7}$$

Here, $f(\theta) = \sin^2\theta$ for the TE- and TM-polarizations in the case of both electric and magnetic material properties. In the non-magnetic case, $f(\theta) = 0$ for the TE- and $f(\theta) = \sin^2\theta$ for the TM-polarization. Note that the $\sin^2\theta$ term in (6.7) and the logarithmic singularity in the denominator agree with the radiation pattern and the impedance of the dipole antenna in Sec. 8.1, see Ref. 4.

The corresponding result for the circular disk of radius a is non-vanishing in the limit as $\xi \to 0$, *viz.*,

$$G_\Lambda B \leq \frac{64\pi^3 a^3}{3\lambda_0^3} f(\theta). \tag{6.8}$$

Here, $f(\theta) = 1 + \cos^2\theta$ for the TE- and TM-polarizations in the case of both electric and magnetic material properties. In the non-magnetic case, $f(\theta) = 1$ for the TE- and and $f(\theta) = \cos^2\theta$ for the TM-polarization. Note the direct application of (6.8) for planar spiral antennas.

7 $\boldsymbol{\gamma}_\infty$ for some generic geometries

In this section, some numerical results of $\boldsymbol{\gamma}_\infty$ are presented and analyzed in terms of the physical limitations discussed in Sec. 3.

7.1 The Platonic solids

Since the Platonic solids are invariant under appropriate point groups, see Ref. 11, their corresponding high-contrast polarizability dyadics $\boldsymbol{\gamma}_\infty$ are isotropic, *i.e.*, $\boldsymbol{\gamma}_\infty = \gamma_\infty \mathbf{I}$, where $\mathbf{I}$ denotes the unit dyadic in $\mathbb{R}^3$. Let $\gamma = \gamma_j$ represent the eigenvalues of $\boldsymbol{\gamma}_\infty$ for $j = 1, 2, 3$. The Platonic solids are depicted in Fig. 6 together with the eigenvalues γ in terms of the volume V of the solids. The five Platonic solids are from left to right the tetrahedron, hexahedron, octahedron, dodecahedron and icosahedron, with 4, 6, 8, 12 and 20 facets, respectively. Included in the figure are also γ in units of $4\pi a^3$, where a denotes the radius of the smallest circumscribing sphere. This comparison with the smallest circumscribing sphere is based on straightforward calculations which is further discussed in Sec. 7.2. The numerical values of γ in Fig. 6 are based on Method of Moments (MoM) calculations, see Ref. 19 and references therein.

Since the upper bound in (3.6) is linear in γ, it follows that among the Platonic solids, the tetrahedron provides the largest upper bound on $G_\Lambda B$ for a given volume V. The eigenvalues γ in Fig. 6 are seen to approach $3V$ as the number of facets increases. This observation is confirmed by the variational principle discussed in Ref. 19, which states that for a given volume the sphere minimizes the trace of $\boldsymbol{\gamma}_\infty$ among all isotropic high-contrast polarizability dyadics. Hence, a lower bound on γ is given by the sphere for which $\gamma = 3V$.

For matched polarizations, the eigenvalues in Fig. 6 can directly be applied to (3.6) to yield an upper bound on the performance of any antenna circumscribed by a given Platonic solid. For example, the non-magnetic tetrahedron yields $G_\Lambda B \leq 624V/\lambda_0^3$ or $G_\Lambda B \leq 0.19$ for $V = 1\,\mathrm{cm}^3$ and center frequency $\mathrm{c}_0/\lambda_0 = 2\,\mathrm{GHz}$. The

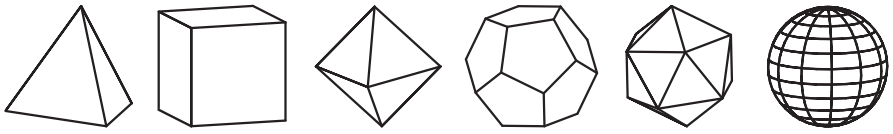

$5.029V$	$3.644V$	$3.551V$	$3.178V$	$3.130V$	$3V$
(0.205)	(0.445)	(0.377)	(0.704)	(0.632)	(1)

Figure 6: The eigenvalues γ (upper row) for the five Platonic solids and the sphere. The number in parenthesis are γ in units of $4\pi a^3$, where a denotes the radius of the smallest circumscribing sphere.

corresponding bound on the quotient D/Q differ only by a factor of π, *i.e.*, $D/Q \leq 0.059$.

It is interesting to note that the pertinent point group symmetries of the Platonic solids are preserved if their geometries are altered appropriately. Such symmetric changes yield a large class of geometries for which $\boldsymbol{\gamma}_\infty$ is isotropic and the upper bound on $G_\Lambda B$ is independent of the polarization. This observation together with the fact that the variational principle discussed above also can be applied to arbitrary isotropic high-contrast polarizability dyadics, are particularly interesting from a MIMO-perspective, see Ref. 9 and references therein.

7.2 Comparison with the sphere

From the discussion of the polarizability dyadics in Ref. 19, it is clear that both γ_1 and γ_2 are directly proportional to the volume of the antenna with a purely geometry dependent proportionality factor. For the circular disk, it follows from Appendix G that even though the volume of the disk vanishes, the eigenvalues γ_1 and γ_2 are non-zero. This result is due to the fact that the geometry dependent proportionality factors $1/L_1$ and $1/L_2$ approach infinity in the limit as the semi-axis ratio approaches zero. In other words, it is not sufficient to only consider the volume part of γ_1 and γ_2 to draw conclusions of the potential in antenna performance for a given volume. In addition, also the shape dependent proportionality factor must be taken into account.

Motivated by the discussion above, it is interesting to compare γ_1 and γ_2 for the different geometries discussed in Secs. 7 and 8, and in Ref. 7. The comparison refers to the smallest circumscribing sphere with radius a, for which γ_1 and γ_2 are equal to $4\pi a^3$, see Ref. 7. For this purpose, introduce $\gamma_1/4\pi a^3$, which, in the case of pure electric material properties, yields a direct measure of the antenna performance in terms of (3.6) and (4.6). The main question addressed in this section is therefore: how much antenna performance can be gained for a given geometry by instead utilizing the full volume of the smallest circumscribing sphere?

In Fig. 7, the goodness number $\gamma_1/4\pi a^3$ are presented for the sphere, circular disk, toroidal ring, and prolate and cylindrical needles, respectively. The generalized

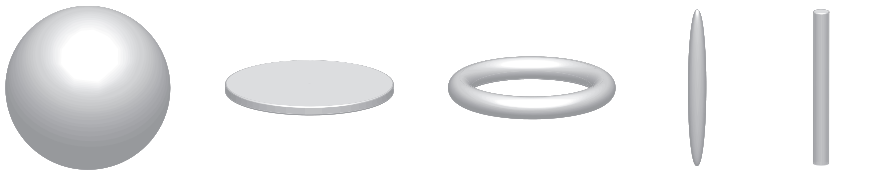

(1) (0.42) (0.24) (0.050) (0.056)

Figure 7: The eigenvalue γ_1 in units of $4\pi a^3$, where a denotes the radius of the smallest circumscribing sphere. The prolate spheroid, the circular ring and the circular cylinder correspond to the generalized semi-axis ratio $\xi = 10^{-3}$.

semi-axis ratio[4] for the toroidal ring and the prolate and cylindrical needles are $\xi = 10^{-3}$. The values for the prolate needle and the toroidal ring are given by (G.3) and (H.5), respectively, while the cylindrical needle is based on FEM simulation for the dipole antenna in Sec. 8.1. The value for the circular disk is $4/3\pi \approx 0.42$ given by (G.4).

The results in Fig. 7 should be compared with the corresponding values in Fig. 6 for the Platonic solids. For example, it is seen that the potential of utilizing the tetrahedron is about 20.5% compared to the smallest circumscribing sphere. Since the high-contrast polarizability dyadics $\boldsymbol{\gamma}_\infty$ are isotropic for the Platonic solids and the sphere, it follows that the results in Fig. 6 also hold for the second and third eigenvalues, γ_2 and γ_3, respectively. This is however not the case for the geometries depicted in Fig. 7 since the circular disk, toroidal ring, and the prolate and cylindrical needles have no isotropic high-contrast polarizability dyadics. For the circular disk and the toroidal ring, γ_1 and γ_2 are equal, and therefore yield the same results as in Fig. 7 for combined electric and magnetic material properties.

In Fig. 7, it is seen that the physical limitations on $G_\Lambda B$ and D/Q for any two-dimensional antenna confined to the circular disk corresponds to about 42% of the potential to utilize the full sphere. This result is rather surprising since, in contrast to the sphere, the circular disk has zero volume. In other words, there is only a factor of $1/0.42 \approx 2.4$ to gain in antenna performance by utilizing three-dimensions compared to two for a given maximum dimension a of the antenna. Since the prolate and cylindrical needles vanish in the limit as the semi-axis ratio approaches zero, the performance of any one-dimensional antenna restricted to the line is negligible as compared to the performance of an antenna in the sphere.

Since γ_1 and γ_2 in the right hand side of (3.6) and (4.6) are determined from separate electric and magnetic problems in the long wavelength limit, see Appendix B, it is clear that electric and magnetic material properties, and hence also γ_1 and γ_2, can be combined separately. For example, any antenna with magnetic properties confined to the circular disk and electric properties confined to the toroidal ring has a potential which is $100(0.42+0.24) = 66\%$ of the sphere with no magnetic material properties present.

[4]The generalized semi-axis ratio for the cylindrical needle and the toroidal ring are defined by $\xi = b/a$, where a and b are given in Figs. 9 and 11, respectively.

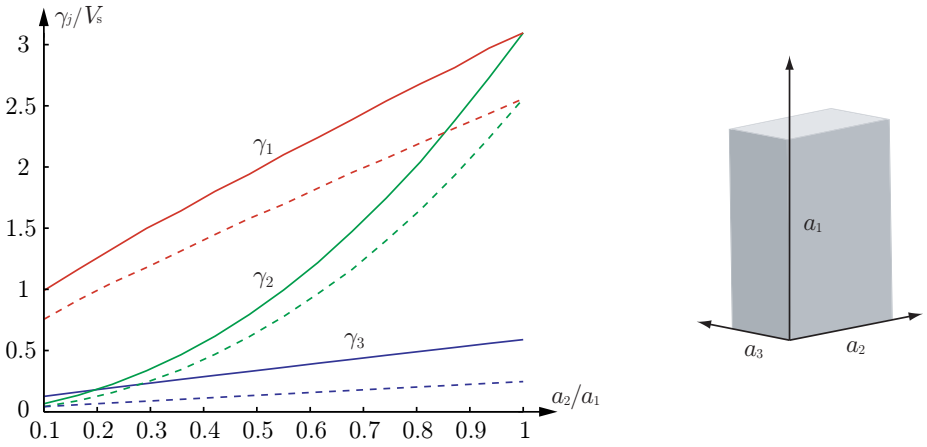

Figure 8: The eigenvalues γ_1, γ_2 and γ_3 as function of the ratio a_2/a_1 for a rectangular parallelepiped of edge lengths a_1, a_2 and a_3. The solid curves are for $a_1/a_3 = 5$ and the dotted curve is for $a_1/a_3 = 10$. Note the normalization with the volume $V_s = \pi a_1^3/6$ of the sphere of radius $a_1/2$.

7.3 The rectangular parallelepiped

The rectangular parallelepiped is a generic geometry that can be used to model, *e.g.*, mobile phones, laptops, and PDAs. The eigenvalues γ_1, γ_2 and γ_3 for a rectangular parallelepiped with edge lengths a_1, a_2 and a_3 are shown in Fig. 8 as a function of the ratio a_2/a_1. The solid and dotted curves correspond to $a_1/a_3 = 5$ and $a_1/a_3 = 10$, respectively. The eigenvalues are ordered $\gamma_1 \geq \gamma_2 \geq \gamma_3$ and the principal axes of the eigenvalues γ_i correspond to the directions parallel to a_i if $a_1 \geq a_2 \geq a_3$. The eigenvalues degenerate if the lengths of the corresponding edges coincide.

The performance of any non-magnetic antenna inscribed in the parallelepiped is limited as shown by (3.5) with $\boldsymbol{\gamma}_m = \mathbf{0}$. Specifically, the limitations on antennas polarized in the a_i direction are given by the eigenvalue, γ_i. Obviously, it is advantageous to utilize the longest dimension of the parallelepiped for the polarization of single port antennas. The limitation (3.5) also quantifies the degradation in using the other directions for the polarization. This is useful for the understanding of fundamental limitations and synthesis of MIMO antennas.

For example, a typical mobile phone is approximately 10 cm high, 5 cm wide, and 1 cm to 2 cm thick. The corresponding eigenvalues γ_1, γ_2 and γ_3 for $a_1 = 10$ cm are seen in Fig. 8 for $a_3 = 2$ cm (solid lines) and $a_3 = 1$ cm (broken lines). The distribution of the eigenvalues γ_1, γ_2 and γ_3 quantifies the trade off between pattern and polarization diversity for multiple antennas systems in the mobile phone. Pattern diversity utilizes the largest eigenvalue but requires an increased directivity at the cost of bandwidth (3.5). Similarly, polarization diversity utilizes at least two eigenvalues. It is observed that it is advantageous to use polarization and pattern diversity for $a_2 \approx a_1$ and $a_2 \ll a_1$, respectively. For a mobile phone where $a_2 \approx a_1/2$, either pattern diversity or a combined pattern and polarization diversity as linear combinations of the a_1 and a_2 directions can be used. Moreover, note that magnetic

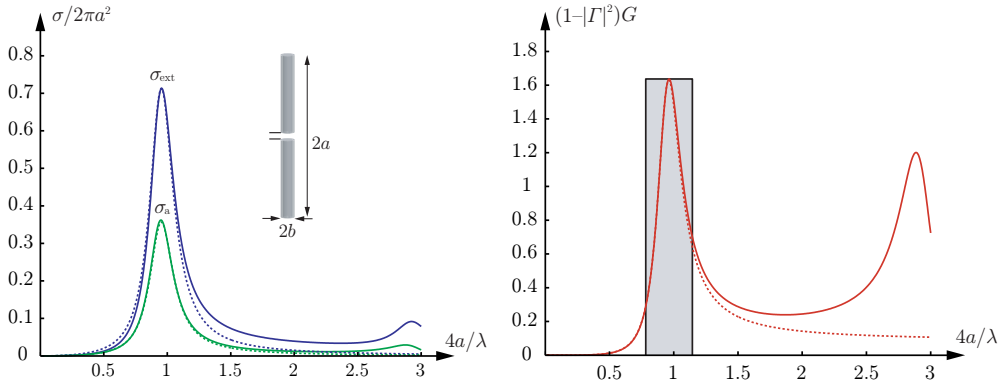

Figure 9: The extinction and absorption cross sections (top figure) and the realized gain (bottom figure) for a cylindrical dipole antenna with axial ratio $b/a = 10^{-3}$. The different curves correspond to Hallén's integral equation (solid curves), directivity and Q-factor limitation (4.6) (dashed curves), and gain and bandwidth limitation (3.6) (shaded box).

materials, increase the bound (3.5) and offer additional possibilities.

8 Analysis of some classical antennas

In this section, numerical simulations of some classical antennas are presented and analyzed in terms of the physical limitations discussed in Sec. 3.

8.1 The dipole antenna

The cylindrical dipole antenna is one of the simplest and most well known antennas. Here, the MoM solution of the Hallén's integral equation in Ref. 10 together with a gap feed model is used to determine the cross sections and impedance for a cylindrical dipole antenna with axial ratio $b/a = 10^{-3}$. The extinction and absorption cross sections and the realized gain are depicted in Fig. 9. The antenna is resonant at $2a \approx 0.48\lambda$ with directivity $D = 1.64$ and radiation resistance $73\,\Omega$. The half-power bandwidth is $B = 25\%$ and the corresponding Q-factor is estimated to $Q = 8.3$ by numerical differentiation of the impedance, see Ref. 25. The absorption efficiency η is depicted in Fig. 10. It is observed that $\eta \approx 0.5$ at the resonance frequency and $\widetilde{\eta} = 0.52$ for $0 \leq 4a/\lambda \leq 3$.

The MoM solution is also used to determine the forward scattering properties of the antenna. The forward scattering is represented by the extinction volume ϱ in Fig. 10. Recall that $\varrho(0)$ and $\operatorname{Im}\varrho$ directly are related to the polarizability dyadics and the extinction cross section, see Sec. 3.

Moreover, since $\operatorname{Re}\varrho \approx 0$ at the resonance frequency, it follows that the real-valued part of the forward scattering is negligible at this frequency. This observation is important in the understanding of the absorption efficiency of antennas, see Ref. 2.

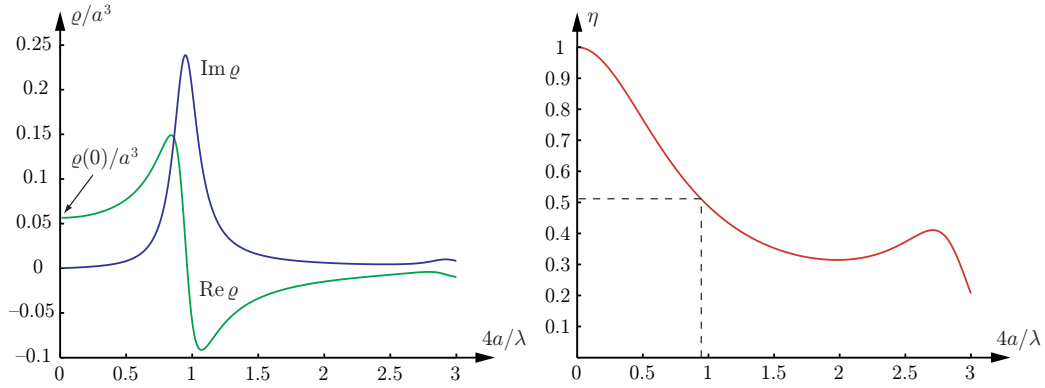

Figure 10: The extinction volume ϱ (top figure) and the absorption efficiency η (bottom figure) as function of $4a/\lambda$ for the dipole antenna.

FEM simulations are used to determine the polarizability dyadic and the eigenvalues of the cylindrical region in Fig. 9. The eigenvalue γ_1, corresponding to a polarization along the dipole, is $\gamma_1 = 0.71a^3$ and the other eigenvalues $\gamma_2 = \gamma_3$ are negligible. The result agrees with the integrated extinction (2.3) of the MoM solution within 2% for $0 \le 4a/\lambda \le 3$.

The eigenvalues $\gamma_1 = 0.71a^3$ and $\gamma_2 = 0$ inserted into (4.6) give physical limitations on the quotient D/Q of any resonant antenna confined to the cylindrical region, *i.e.*,

$$\sup_{\hat{\boldsymbol{p}}_{\rm e}\cdot\hat{\boldsymbol{p}}_{\rm m}=0} \frac{D}{Q} \le \widetilde{\eta}\frac{k_0^3\gamma_1}{2\pi} \approx 0.39\widetilde{\eta}. \tag{8.1}$$

The corresponding bound on the Q-factor is $Q \ge 8.1$, if $D = 1.64$ and $\widetilde{\eta} = 0.52$ are used. In Fig. 9, it is observed that the single resonance model (dashed curves) with $Q = 8.5$ is a good approximation of the cross sections and realized gain. The corresponding half-power bandwidth is 24%. The eigenvalue γ_1 also gives a limitation on the product $G_\Lambda B$ in (3.6) as illustrated with the rectangular region in the right figure for an arbitrary minimum scattering antenna ($\widetilde{\eta} = 0.5$). The realized gain $G_\Lambda = 1.64$ gives the relative bandwidth $B = 38\%$.

It is also illustrative to compare the physical limitations with the MoM simulation for a short dipole. The resonance frequency of the dipole is reduced to $2a \approx 0.2\lambda$ with an inductive loading of $5\,\mu$H connected in series with the dipole. The MoM impedance computations of the short dipole give the half-power bandwidth $B = 1.4\%$ and the radiation resistance $8\,\Omega$. The D/Q bound (4.6) gives $Q \ge 110$ for the directivity $D = 1.52$ and an absorption efficiency $\widetilde{\eta} = 1/2$ corresponding to the half-power bandwidth $B \le 1.8\%$.

Obviously, the simple structure of the dipole and the absence of broadband matching networks make the resonance model favorable. The limitation (4.6) is in excellent agreement with the performance of the dipole antenna for the absorption efficiency $\widetilde{\eta} = 0.52$, *i.e.*, $Q \ge 8.1$ from (4.6) compared to $Q = 8.3$ from the MoM solution. The $G_\Lambda B$ bound overestimates the bandwidth, but a broadband matching

network can be used to enhance the bandwidth of the dipole, see Ref. 5.

Observe that the dipole antenna has a circumscribing sphere with $ka \approx 1.5$ and is not considered electrically small according to the Chu limitations in Ref. 3. The corresponding limit for the $2a \approx 0.2\lambda_0$ dipole ($ka \approx 0.63$ and $D = 1.52$) is $Q \geq 5.6$ and the half-power bandwidth of $36\% \gg 1.4\%$. In conclusion, the dipole utilizes the cylindrical region very efficiently but obviously not the spherical region.

8.2 The loop antenna

The magnetic counterpart to the dipole antenna in Sec. 8.1 is the loop antenna. The geometry of the loop antenna is conveniently described in toroidal coordinates, see Sec. H. Laplace's equation separates in the toroidal coordinate system and hence permits an explicit calculation of the high-contrast polarizability dyadic $\boldsymbol{\gamma}_\infty$. In this section the attention is restricted to the loop antenna of vanishing thickness and non-magnetic material properties. Under the assumptions of vanishing thickness, the analysis in Sec. H yields closed-form expressions of the eigenvalues γ_1, γ_2 and γ_3. Recall that the loop antenna coincides with the magnetic dipole in the long wavelength limit $a/\lambda \ll 1$.

In order to quantify the vanishing thickness limit, introduce the semi-axis ratio $\xi = b/a$, where a and b denote the axial and cross section radii, respectively, see Fig. 11. The three eigenvalues $\gamma_1 = \gamma_2$ and γ_3 are seen to vanish in the limit $\xi \to 0$. However, γ_1 and γ_2 vanish slower than γ_3, see Sec. H. The eigenvalues in the limit $\xi \to 0$ inserted into (4.5) yields

$$\frac{D}{Q} \leq \pi k_0^3 a^3 \frac{f(\theta)}{\ln 2/\xi - 1} + \mathcal{O}(\xi^2) \quad \text{as } \xi \to 0, \tag{8.2}$$

where $f(\theta) = 1$ for the TE- and $f(\theta) = \cos^2\theta$ for the TM-polarization. Here, $\theta \in [0, \pi]$ is the polar angle measured from the z-axis of symmetry in Fig. 11. Note that the logarithmic singularity in (8.2) is the same as for the dipole antenna, see Sec. H. Since the axial radius a is the only length scale that is present in the loop antenna in the limit $\xi \to 0$, it is natural that γ_1, γ_2, and γ_3 are proportional to a^3, see Appendix B.

By comparing the discussion above with the results in Ref. 7 and Sec. 8.1, it is concluded that there is a strong equivalence between the electric and magnetic dipoles. For the most advantageous polarization the upper bound on $G_\Lambda B$ is a factor of $3\pi/2$ larger for the loop antenna compared to the electric dipole.

The results are exemplified for a self-resonant loop with $k_0 a = 1.1$ and a capacitively loaded loop, $C = 10\,\text{pF}$, with $k_0 a = 0.33$, both with $\xi = 0.01$. The corresponding limitations (4.6) are $D/Q \leq 0.95\bar{\eta}$ and $D/Q \leq 0.025\bar{\eta}$, respectively. The MoM is used to determine the impedance and realized gain of the loop antenna with a gap feed at $\phi = 0$, see Fig. 11. The Q-factor of the self-resonant antenna is estimated to $Q = 5$ from numerical differentiation of the impedance, see Ref. 25. The corresponding main beam is in the $\hat{\boldsymbol{z}}$-direction with a directivity $D = 2.36$ giving $D/Q = 0.47$. Similarly, the tuned loop has $Q \approx 164$ and $D = 1.43$ in $\theta = 90^\circ$ and $\phi = 90^\circ$ giving $D/Q \approx 0.0086$.

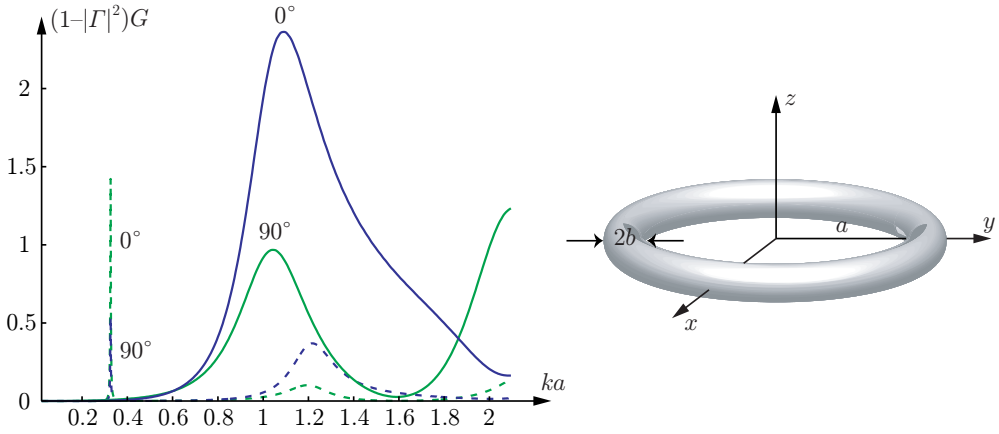

Figure 11: The realized partial gain of two loop antennas for $\theta = 0°, 90°$. One self resonant ($ka \approx 1$) and one capacitively tuned to $ka \approx 1/3$.

It is observed that the physical limitations (4.6) of the loops agree well with the MoM results. This difference can be reduced by introducing the appropriate absorption efficiency in the physical limitation. The corresponding results for the Chu limitation are $D/Q \leq 2.3$ for $k_0 a = 1.1$ and $D/Q \leq 0.18$ for $k_0 a = 0.33$, where the combined TE- and TM-case have been used as the loops are not omnidirectional, see Refs. 3 and 12.

8.3 Conical antennas

The bandwidth of a dipole antenna increases with the thickness of the antenna. The bandwidth can also be increased with conical dipoles, *i.e.*, the biconical antenna. The corresponding conical monopole and discone antennas are obtained by replacing one of the cones with a ground plane, see Ref. 21.

In Fig. 12, the eigenvalues $\gamma_x = \gamma_y$ and γ_z, corresponding to horizontal and vertical polarizations, respectively, are shown as a function of the ground plane radius, b, for the conical monopoles with angles $\theta = 10°$ and $30°$. The eigenvalues are normalized with a^3, where a is the height of the cone. It is observed that the eigenvalues increase with the radius, b, of the ground plane and the cone angle θ. This is a general result as the polarizability dyadic is non-decreasing with increasing susceptibilities, see Ref. 19.

The horizontal eigenvalues $\gamma_x = \gamma_y$ are dominated by the ground plane and increase approximately as b^3 according to the polarizability of the circular disk, see Appendix C. The vertical eigenvalue γ_z approaches $\gamma_{bz}/2$ as $b \to \infty$, where γ_{bz} denotes the vertical eigenvalue of the corresponding biconical antenna.

It is interesting to compare the D/Q estimate (4.6) for the biconical antenna and conical monopole antenna with a large but finite ground plane. The vertical eigenvalue γ_z of the conical monopole antenna is approximately half of the corresponding eigenvalue of the biconiocal antenna and the Q-factors of the two antennas are similar. The physical limitation on the directivity in the $\theta = 90°$-direction of

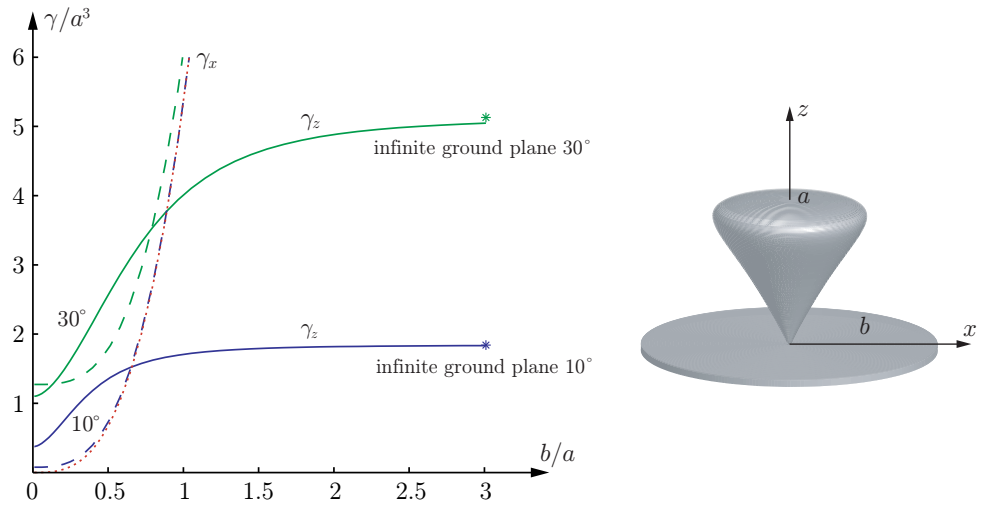

Figure 12: The vertical and horizontal eigenvalues γ_z and γ_x as function of the radius b for a biconical antenna of half vertex angle 10° and 30°, respectively.

the conical monopole is hence half of the directivity of the corresponding biconical antenna. This might appear contradictory as it is well known that the maximal directivity of a monopole is approximately twice the directivity of the corresponding dipole. However, the $\theta = 90°$-direction is on the border between the illuminated and the shadow regions. The integral representation of the far field shows that the induced ground-plane currents do not contribute to the far field in this direction, implying that the directivity is reduced a factor of four as suggested by the physical limitations, see Appendix D.

The rapid increase in $\gamma_x = \gamma_y$ with the radius of the ground plane suggests that it is advantageous to utilize the polarization in the theses directions. This is done by the discone antenna that has an omnidirectional pattern with a maximal directivity above $\theta = 90°$.

9 Conclusion and future work

In this paper, physical limitations on reciprocal antennas of arbitrary shape are derived based on the holomorphic properties of the forward scattering dyadic. The results are very general in the sense that the underlying analysis solely depends on energy conservation and the fundamental principles of linearity, time-translational invariance, and causality. Several deficiencies and drawbacks of the classical limitations of Chu and Wheeler in Refs. 3 and 24 are overcomed with this new formulation. The main advantages of the new limitations are at least fivefold: 1) they hold for arbitrary antenna geometries; 2) they are formulated in the gain and bandwidth as well as the directivity and the Q-factor; 3) they permit study of polarization effects such as diversity in applications for MIMO communication systems; 4) they successfully separate electric and magnetic antenna properties in terms of the in-

trinsic material parameters; 5) they are isoperimetric from a practical point of view in the sense that for some geometries, physical antennas can be realized which yield equality in the limitations.

The main results of the present theory are the limitations on the partial realized gain and partial directivity in (3.4) and (4.5), respectively. Since the upper bounds in (3.4) and (4.5) are proportional to $k_0^3 a^3$, where a denotes the radius of, say, the volume equivalent sphere, it is clear that no broadband electrically small antennas exist unless gain or directivity is sacrificed for bandwidth or Q-factor. This is also the main conclusion in Ref. 12, but there presented on more vague grounds. Furthermore, the present theory suggests that, in addition to electric material properties, also magnetic materials could be invoked in the antenna design to increase the performance, *cf.*, the ferrite loaded loop antenna in Ref. 4.

In contrast to the classical results by Chu and Wheeler in Refs. 3 and 24, these new limitations are believed to be isoperimetric in the sense that the bounds hold for some physical antenna. A striking example of the intrinsic accuracy of the theory is illustrated by the dipole antenna in Sec. 8.1. In fact, many wire antennas are believed to be close to the upper bounds since these antennas make effective use of their volumes.

It is important to remember that a priori knowledge of the absorption efficiency $\eta = \sigma_{\mathrm{a}}/\sigma_{\mathrm{ext}}$ can sharpen the bounds in (3.4) and (4.5), *cf.*, the half-wave dipole antenna in Sec. 8.1 for which $\widetilde{\eta} \approx 1/2$ is used. Similarly, a priori knowledge of the radiation efficiency, η_{r}, can be used to improve the estimate in (3.2) using $G = \eta_{\mathrm{r}} D$.

The performance of an arbitrary antenna can be compared with the upper bounds in Secs. 3 and 4 using either the method of moments (MoM) or the finite difference time domain method (FDTD). For such a comparison, it is beneficial to determine the integrated extinction and compare the result using (2.3) rather than (3.4) and (4.5). The reason for this is that the full absorption and scattering properties are contained within (2.3) in contrast to (3.4) and (4.5). In fact, (2.3) is the fundamental physical relation and should be the starting point of much analysis.

In addition to the broadband absorption efficiency $\widetilde{\eta}$, several implications of the present theory remains to investigate. Future work include the effect of non-simple connected geometries (array antennas) and its relation to capacitive coupling, and additional analysis of classical antennas. From a wireless communication point of view it is also interesting to investigate the connection between the present theory and the concept of correlation and capacity in MIMO communication systems. Some of the problems mentioned here will be addressed in forthcoming papers.

Acknowledgment

The financial support by the Swedish Research Council and the SSF Center for High Speed Wireless Communication are gratefully acknowledged. The authors are also grateful for fruitful discussions with Anders Karlsson and Anders Derneryd at Dept. of Electrical and Information Technology, Lund University, Sweden.

Appendix A Details on the derivation of (2.3)

Consider a plane-wave excitation $\boldsymbol{E}_{\mathrm{i}}(\mathrm{c}_0 t - \hat{\boldsymbol{k}} \cdot \boldsymbol{x})$ incident in the $\hat{\boldsymbol{k}}$-direction, see Fig. 1. In the far field region, the scattered electric field $\boldsymbol{E}_{\mathrm{s}}$ is described by the far field amplitude $\boldsymbol{F}$ as

$$\boldsymbol{E}_{\mathrm{s}}(t, \boldsymbol{x}) = \frac{\boldsymbol{F}(\mathrm{c}_0 t - x, \hat{\boldsymbol{x}})}{x} + \mathcal{O}(x^{-2}) \quad \text{as } x \to \infty, \tag{A.1}$$

where c_0 denotes the speed of light in vacuum, and $\hat{\boldsymbol{x}} = \boldsymbol{x}/x$ with $x = |\boldsymbol{x}|$. The far field amplitude $\boldsymbol{F}$ in the forward direction $\hat{\boldsymbol{k}}$ is assumed to be causal and related to the incident field $\boldsymbol{E}_{\mathrm{i}}$ via the linear and time-translational invariant convolution

$$\boldsymbol{F}(\tau, \hat{\boldsymbol{k}}) = \int_{-\infty}^{\tau} \mathbf{S}_{\mathrm{t}}(\tau - \tau', \hat{\boldsymbol{k}}, \hat{\boldsymbol{k}}) \cdot \boldsymbol{E}_{\mathrm{i}}(\tau') \, \mathrm{d}\tau'.$$

Here, $\tau = \mathrm{c}_0 t - x$ and $\mathbf{S}_{\mathrm{t}}$ is the appropriate dimensionless temporal dyadic.

Introduce the forward scattering dyadic $\mathbf{S}$ as the Fourier transform of $\mathbf{S}_{\mathrm{t}}$ evaluated in the forward direction, *i.e.*,

$$\mathbf{S}(k, \hat{\boldsymbol{k}}) = \int_{0^-}^{\infty} \mathbf{S}_{\mathrm{t}}(\tau, \hat{\boldsymbol{k}}, \hat{\boldsymbol{k}}) \mathrm{e}^{\mathrm{i}k\tau} \, \mathrm{d}\tau, \tag{A.2}$$

where k is complex-valued with $\operatorname{Re} k = \omega/\mathrm{c}_0$. Recall that $\mathbf{S}(\mathrm{i}k, \hat{\boldsymbol{k}})$ is real-valued for real-valued k and that the crossing symmetry $\mathbf{S}(k, \hat{\boldsymbol{k}}) = \mathbf{S}^*(-k^*, \hat{\boldsymbol{k}})$ holds for complex-valued k. For a large class of temporal dyadics $\mathbf{S}_{\mathrm{t}}$, the elements of $\mathbf{S}$ are holomorphic in the upper half plane $\operatorname{Im} k > 0$.

From the analysis above, it follows that the Fourier transform of (A.1) in the forward direction reads

$$\boldsymbol{E}_{\mathrm{s}}(k, x\hat{\boldsymbol{k}}) = \frac{\mathrm{e}^{\mathrm{i}kx}}{x} \mathbf{S}(k, \hat{\boldsymbol{k}}) \cdot \boldsymbol{E}_0 + \mathcal{O}(x^{-2}) \quad \text{as } x \to \infty,$$

where $\boldsymbol{E}_0$ is the Fourier amplitude of the incident field. Introduce the extinction volume $\varrho(k) = \hat{\boldsymbol{p}}_{\mathrm{e}}^* \cdot \mathbf{S}(k, \hat{\boldsymbol{k}}) \cdot \hat{\boldsymbol{p}}_{\mathrm{e}}/k^2$, where $\hat{\boldsymbol{p}}_{\mathrm{e}} = \boldsymbol{E}_0/|\boldsymbol{E}_0|$ and $\hat{\boldsymbol{p}}_{\mathrm{m}} = \hat{\boldsymbol{k}} \times \hat{\boldsymbol{p}}_{\mathrm{e}}$ denote the electric and magnetic polarizations, respectively. Since the elements of $\mathbf{S}$ are holomorphic in k for $\operatorname{Im} k > 0$, it follows that also the extinction volume ϱ is a holomorphic function in the upper half plane. The Cauchy integral theorem with respect to the contour in Fig. 13 then yields

$$\varrho(\mathrm{i}\varepsilon) = \int_0^{\pi} \frac{\varrho(\mathrm{i}\varepsilon - \varepsilon \mathrm{e}^{\mathrm{i}\phi})}{2\pi} \, \mathrm{d}\phi + \int_0^{\pi} \frac{\varrho(\mathrm{i}\varepsilon + R\mathrm{e}^{\mathrm{i}\phi})}{2\pi} \, \mathrm{d}\phi + \int_{\varepsilon < |k| < R} \frac{\varrho(k + \mathrm{i}\varepsilon)}{2\pi \mathrm{i} k} \, \mathrm{d}k. \tag{A.3}$$

Here, it is assumed that the extinction volume ϱ is sufficiently regular to extend the contour to the real-axis in the last integral on the right hand side of (A.3). Relation (A.3) is subject to the limits as $\varepsilon \to 0$ and $R \to \infty$.

The left hand side of (A.3) and the integrand in the first integral on the right hand side are well-defined in the limit as $\varepsilon \to 0$. For a sufficiently regular ϱ in the vicinity of the origin, the analysis in Ref. 14 yield

$$\varrho(\mathrm{i}\varepsilon) = \frac{1}{4\pi} (\hat{\boldsymbol{p}}_{\mathrm{e}}^* \cdot \boldsymbol{\gamma}_{\mathrm{e}} \cdot \hat{\boldsymbol{p}}_{\mathrm{e}} + \hat{\boldsymbol{p}}_{\mathrm{m}}^* \cdot \boldsymbol{\gamma}_{\mathrm{m}} \cdot \hat{\boldsymbol{p}}_{\mathrm{m}}) + \mathcal{O}(\varepsilon) \quad \text{as } \varepsilon \to 0. \tag{A.4}$$

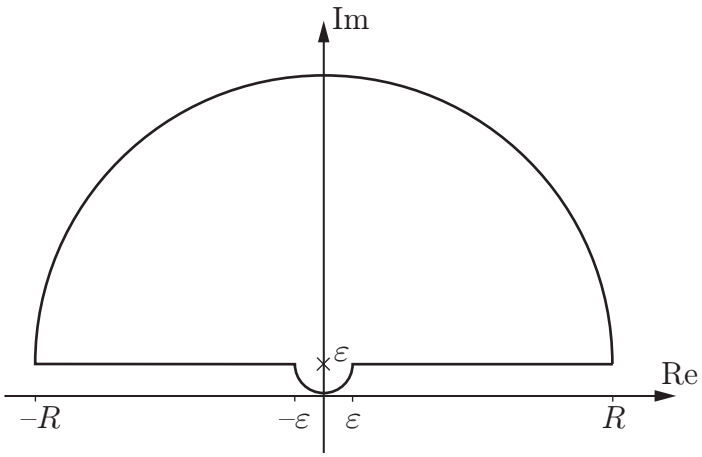

Figure 13: Integration contour in the complex k-plane used in (A.3).

Here, $\boldsymbol{\gamma}_{\mathrm{e}}$ and $\boldsymbol{\gamma}_{\mathrm{m}}$ denote the electric and magnetic polarizability dyadics in Appendix B. Since the short wavelength response of a material is non-unique from a modeling point of view, see Ref. 8, the second term on the right hand side of (A.3) is assumed to approach zero in the limit $R \to \infty$. In fact, for a large class of temporal dyadics $\mathbf{S}_{\mathrm{t}}$, the integrand $\varrho(\mathrm{i}\varepsilon + R\mathrm{e}^{\mathrm{i}\phi})/2\pi$ is proportional to the projected area A in the forward direction, *viz.*,

$$\varrho(k) = -\frac{A(\hat{\boldsymbol{k}})}{2\pi \mathrm{i}k} + \mathcal{O}(|k|^{-2}) \quad \text{as } |k| \to \infty, \qquad \mathrm{Im}\, k \geq 0. \tag{A.5}$$

The asymptotic behavior (A.5) is known as the extinction paradox, see Ref. 23. The constant A is real-valued since $\mathbf{S}(\mathrm{i}k, \hat{\boldsymbol{k}})$ is real-valued for real-valued k.

In order to proceed, the scattering, absorption and extinction cross sections are introduced. The scattering cross section σ_{s} and absorption cross section σ_{a} are defined as the ratio of the scattered and absorbed power, respectively, to the incident power flow density in the forward direction. The sum of the scattering and absorption cross sections is the extinction cross section $\sigma_{\mathrm{ext}} = \sigma_{\mathrm{s}} + \sigma_{\mathrm{a}}$. The three cross sections σ_{s}, σ_{a} and σ_{ext} are by definition real-valued and non-negative. The principle of energy conservation takes the form as a relation between the extinction volume ϱ and the extinction cross section. The relation is known as the optical theorem, see Refs. 16 and 22,

$$\sigma_{\mathrm{ext}}(k) = 4\pi k\, \mathrm{Im}\, \varrho(k), \tag{A.6}$$

where k is real-valued.

In summary, the real part of (A.3) subject to the limits $\varepsilon \to 0$ and $R \to \infty$ yields

$$\varrho(0) = \frac{1}{\pi} \int_{-\infty}^{\infty} \frac{\mathrm{Im}\, \varrho(k)}{k}\, \mathrm{d}k. \tag{A.7}$$

The optical theorem (A.6) applied to (A.7) then implies

$$\varrho(0) = \frac{1}{4\pi^2} \int_{-\infty}^{\infty} \frac{\sigma_{\mathrm{ext}}(k)}{k^2}\, \mathrm{d}k = \frac{1}{4\pi^3} \int_{0}^{\infty} \sigma_{\mathrm{ext}}(\lambda)\, \mathrm{d}\lambda, \tag{A.8}$$

where the wavelength $\lambda = 2\pi/k$ has been introduced. Hence, invoking (A.4) finally yields the integrated extinction

$$\int_0^\infty \sigma_{\text{ext}}(\lambda)\ \mathrm{d}\lambda = \pi^2 \left(\hat{\boldsymbol{p}}_{\text{e}}^* \cdot \boldsymbol{\gamma}_{\text{e}} \cdot \hat{\boldsymbol{p}}_{\text{e}} + \hat{\boldsymbol{p}}_{\text{m}}^* \cdot \boldsymbol{\gamma}_{\text{m}} \cdot \hat{\boldsymbol{p}}_{\text{m}}\right). \tag{A.9}$$

In fact, the already weak assumptions on the extinction volume ϱ in the analysis above can be relaxed via the introduction of certain classes of distributions, see Ref. 17.

Appendix B The polarizability dyadics

Let $\boldsymbol{\tau}$ denote a finite material dyadic ($\boldsymbol{\chi}_{\text{e}}$ without a conductivity term, or $\boldsymbol{\chi}_{\text{m}}$) with compact support. The entries of the polarizability dyadic $\boldsymbol{\gamma}$ ($\boldsymbol{\gamma}_{\text{e}}$ or $\boldsymbol{\gamma}_{\text{m}}$ depending on whether the problem is electric or magnetic) are defined as the volume integral

$$\hat{\boldsymbol{e}}_i \cdot \boldsymbol{\gamma} \cdot \hat{\boldsymbol{e}}_j = \frac{1}{E_0} \hat{\boldsymbol{e}}_i \cdot \int_{\mathbb{R}^3} \boldsymbol{\tau}(\boldsymbol{x}) \cdot \boldsymbol{E}_j(\boldsymbol{x})\ \mathrm{dV}_{\boldsymbol{x}}, \qquad i,j = 1,2,3. \tag{B.1}$$

Here, the total field $\boldsymbol{E}$ has been decomposed as $\boldsymbol{E}_j = E_0 \hat{\boldsymbol{e}}_j + \boldsymbol{E}_{\text{s}j}$ with respect to the mutually orthonormal vectors $\hat{\boldsymbol{e}}_j$. In the electric and magnetic cases, $\boldsymbol{E}$ represents the electric and magnetic field, respectively.

In the high-contrast limit, when the entries of $\boldsymbol{\tau}$ simultaneously approach infinity uniformly in $\boldsymbol{x}$, the pertinent definition of the high-contrast polarizability dyadic $\boldsymbol{\gamma}_\infty$ is, see Ref. 14,

$$\hat{\boldsymbol{e}}_i \cdot \boldsymbol{\gamma}_\infty \cdot \hat{\boldsymbol{e}}_j = \frac{1}{E_0} \hat{\boldsymbol{e}}_i \cdot \sum_{n=1}^{N} \int_{\mathrm{S}_n} \left(\hat{\boldsymbol{\nu}}(\boldsymbol{x}) \Phi_j(\boldsymbol{x}) - \boldsymbol{x} \hat{\boldsymbol{\nu}}(\boldsymbol{x}) \cdot \nabla \Phi_j(\boldsymbol{x})\right)\ \mathrm{dS}_{\boldsymbol{x}}. \tag{B.2}$$

The surface integral representation (B.2) holds for N disjunct bounding surfaces S_n with outward-directed unit normal vectors $\hat{\boldsymbol{\nu}}$. The potential $\Psi_j(\boldsymbol{x}) = \Phi_j(\boldsymbol{x}) - E_0 x_j$ is for each $n = 1, 2, \ldots, N$ the solution to the boundary value problem

$$\begin{cases} \nabla^2 \Psi_j(\boldsymbol{x}) = 0, \quad \boldsymbol{x} \text{ outside } \mathrm{S}_n \\ \displaystyle\int_{\mathrm{S}_n} \hat{\boldsymbol{\nu}}(\boldsymbol{x}) \cdot \nabla \Psi_j(\boldsymbol{x}) \mid_+ \ \mathrm{dS}_{\boldsymbol{x}} = 0 \\ \Psi_j(\boldsymbol{x}) \to -E_0 x_j + \mathcal{O}(|\boldsymbol{x}|^{-2}) \quad \text{as } |\boldsymbol{x}| \to \infty \end{cases}$$

The presence of a finite or infinite conductivity term in $\boldsymbol{\chi}_{\text{e}}$ is discussed in Ref. 14. The conclusion is that the electric polarizability dyadic $\boldsymbol{\gamma}_{\text{e}}$ should be replaced by $\boldsymbol{\gamma}_\infty$ independently of the real-part of $\boldsymbol{\chi}_{\text{e}}$ when a conductivity term is present. This may at first seem contradictory, since there is no continuity in the limit as the conductivity vanishes.

In Ref. 19, the polarizability dyadic $\boldsymbol{\gamma}$ is proved to be symmetric provided $\boldsymbol{\tau}$ is symmetric at all points $\boldsymbol{x}$. The dyadic $\boldsymbol{\gamma}$ is real-valued, and hence diagonalizable with real-valued eigenvalues. The corresponding set of orthogonal eigenvectors are

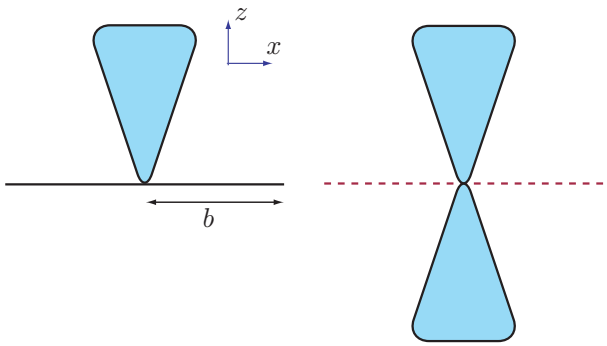

Figure 14: Illustration of an arbitrary antenna volume supported by a ground plane (left figure) and its corresponding mirror object (right figure).

the principal axes of the obstacle under consideration. The principal axes are particularly easy to determine for obstacles with continuous or discrete symmetries, *e.g.*, the ellipsoids and the Platonic solids in Sec. 7.1.

An important property of $\boldsymbol{\gamma}$ which is proved in Ref. 19, is that it is proportional to the volume of the support of $\boldsymbol{\tau}$. This is a direct consequence of the absence of any length scales in the long wavelength limit.

Appendix C Supporting ground planes

Supporting ground planes are central structures in many antenna applications. Consider an arbitrary volume, modeling the antenna, situated above a supporting ground plane of finite or infinite extent, see Fig. 14. To simplify the terminology, use monopole to denote object with a ground plane and dipole to denote the object together with its mirror object. The ground plane is assumed to be a circular disk of radius b with vanishing thickness. Since $\boldsymbol{\gamma}_\infty$ is independent of any coordinate representation, let the ground plane be given by $z = 0$.

For a polarization parallel with the ground plane, *i.e.*, spanned by $\hat{\boldsymbol{e}}_x$ and $\hat{\boldsymbol{e}}_y$, it is clear from the results in Appendix B of the circular disk that the contribution to $\boldsymbol{\gamma}_\infty$ from the ground plane is large. Indeed, a circular ground plane of radius b yields $\gamma_{\mathrm{x}} = \gamma_{\mathrm{y}} = 16b^3/3$, where γ_{x} and γ_{y} denote the eigenvalues of $\boldsymbol{\gamma}_\infty$ corresponding to the $\hat{\boldsymbol{e}}_x$ and $\hat{\boldsymbol{e}}_y$ directions, respectively (G.4).

The polarizability of the monopole for an electric polarization parallel with the $\hat{\boldsymbol{e}}_z$-direction has one contribution from the charge distribution on the object $z > 0$ and one part from the charge distribution on the ground plane $z = 0$. The contribution from the ground plane vanishes in (B.2) since $z = 0$. For a ground plane of infinite extent the method of images is applicable to determine the charge distribution for $z > 0$. In this method, the ground plane is replaced with a copy of the object placed in the mirror position of the object, *i.e.*, the dipole. The charge distribution is odd in z and the charge distribution for $z > 0$ is identical in the monopole and dipole cases. The polarizability of the dipole is hence exactly twice

the polarizability of the corresponding monopole.

The difference between the finite and infinite ground planes is negligible as long as the charge distribution on the monopole can be approximated by the charge distribution in the corresponding dipole case.

Appendix D Directivity along ground planes

The integral representation of the far-field can be used to analyze the directivity of antennas in directions along the supporting ground plane. The pertinent integral representation reads

$$\boldsymbol{F}(\hat{\boldsymbol{r}}) = \frac{\mathrm{i}kZ_0}{4\pi} \int_S \hat{\boldsymbol{r}} \times (\boldsymbol{J}(\boldsymbol{x}) \times \hat{\boldsymbol{r}}) \mathrm{e}^{-\mathrm{i}k\hat{\boldsymbol{r}}\cdot\boldsymbol{x}} \, \mathrm{dS}_{\boldsymbol{x}}, \tag{D.1}$$

where $\boldsymbol{J}$ and Z_0 denote the induced current and the free space impedance, respectively.

Consider a monopole, *i.e.*, an object on a large but finite ground plane, at $z = 0$ with $\hat{\boldsymbol{e}}_z$ as a symmetry axis, see Fig. 14. The far-field of the monopole (D.1) can be written as a sum of one integral over the ground plane and one integral over the object. Let S_+ and S_0 denote the corresponding surfaces of the object and the ground plane, respectively. Assume that the ground plane is sufficiently large such that the currents on the monopole can be approximated with the currents on the corresponding dipole case for $z > 0$. Moreover, assume that the current is rotationally symmetric and that the current in the ϕ-direction is negligible giving an omni-directional radiation pattern. Hence, it is sufficient to consider the far-field pattern in the $\hat{\boldsymbol{r}} = \hat{\boldsymbol{e}}_x$-direction.

The induced currents on the ground plane are in the radial direction giving the term $\hat{\boldsymbol{e}}_x \times (\boldsymbol{J}(\boldsymbol{x}) \times \hat{\boldsymbol{e}}_x) = \hat{\boldsymbol{e}}_y J_\rho(\rho) \sin\phi$ in (D.1). It is seen that the currents on the ground plane does not contribute to the far field as

$$\boldsymbol{F}(\hat{\boldsymbol{e}}_x) = \hat{\boldsymbol{e}}_y \frac{\mathrm{i}k\eta}{4\pi} \int_{S_0} \mathrm{e}^{-\mathrm{i}k\rho\cos\phi} J_\rho(\rho) \sin\phi\rho \, \mathrm{d}\phi \, \mathrm{d}\rho = \boldsymbol{0}. \tag{D.2}$$

The contribution from the currents on the object can be analyzed with the method of images. From (D.2), it is seen the it is only the currents in the $\hat{\boldsymbol{e}}_z$-direction that contributes to the far field, *i.e.*,

$$\boldsymbol{F}(\hat{\boldsymbol{e}}_x) = \hat{\boldsymbol{e}}_z \frac{\mathrm{i}k\eta}{4\pi} \int_{S_+} \mathrm{e}^{-\mathrm{i}k\rho\cos\phi} J_z(\rho, z) \, \mathrm{dS}, \tag{D.3}$$

where $J_z\hat{\boldsymbol{e}}_z = \hat{\boldsymbol{e}}_x \times (\boldsymbol{J} \times \hat{\boldsymbol{e}}_x)$. The method of images shows that J_z is even in z so the z-directed currents above and below the ground plane give equal contributions to the far field. The directivity of the monopole antenna is hence a quarter of the directivity of the corresponding dipole antenna in the $\hat{\boldsymbol{e}}_x$-direction.

Appendix E Definition of some antenna terms

The following definitions of antenna terms are based on the IEEE standard 145-1993 in Ref. 13. The definitions refer to the electric polarization $\hat{\boldsymbol{p}}_{\mathrm{e}}$ (co-polarization) rather than the magnetic polarization $\hat{\boldsymbol{p}}_{\mathrm{m}} = \hat{\boldsymbol{k}} \times \hat{\boldsymbol{p}}_{\mathrm{e}}$ (cross-polarization). The antennas are assumed to reciprocal, *i.e.*, they have similar properties as transmitting and receiving devices.

Absolute gain $G(\hat{\boldsymbol{k}})$**.** The absolute gain is the ratio of the radiation intensity in a given direction to the intensity that would be obtained if the power accepted by the antenna was radiated isotropically.

Partial gain $G(\hat{\boldsymbol{k}}, \hat{\boldsymbol{p}}_{\mathrm{e}})$**.** The partial gain in a given direction is the ratio of the part of the radiation intensity corresponding to a given polarization to the radiation intensity that would be obtained if the power accepted by the antenna was radiated isotropically. The absolute gain is equal to the sum of the partial gains for two orthogonal polarizations, *i.e.*, $G(\hat{\boldsymbol{k}}) = G(\hat{\boldsymbol{k}}, \hat{\boldsymbol{p}}_{\mathrm{e}}) + G(\hat{\boldsymbol{k}}, \hat{\boldsymbol{p}}_{\mathrm{m}})$.

Realized gain $G(\hat{\boldsymbol{k}}, \Gamma)$**.** The realized gain is the absolute gain of an antenna reduced by the losses due to impedance mismatch of the antenna, *i.e.*, $G(\hat{\boldsymbol{k}}, \Gamma) = (1 - |\Gamma|^2) G(\hat{\boldsymbol{k}})$.

Partial realized gain $G(\hat{\boldsymbol{k}}, \hat{\boldsymbol{p}}_{\mathrm{e}}, \Gamma)$**.** The partial realized gain is the partial gain for a given polarization reduced by the losses due to impedance mismatch of the antenna, *i.e.*, $G(\hat{\boldsymbol{k}}, \hat{\boldsymbol{p}}_{\mathrm{e}}, \Gamma) = (1 - |\Gamma|^2) G(\hat{\boldsymbol{k}}, \hat{\boldsymbol{p}}_{\mathrm{e}})$.

Absolute directivity $D(\hat{\boldsymbol{k}})$**.** The absolute directivity is the ratio of the radiation intensity in a given direction to the radiation intensity averaged over all directions. The averaged radiation intensity is equal to the total power radiated divided by 4π.

Partial directivity $D(\hat{\boldsymbol{k}}, \hat{\boldsymbol{p}}_{\mathrm{e}})$**.** The partial directivity in a given direction is the ratio of that part of the radiation intensity corresponding to a given polarization to the radiation intensity averaged over all directions. The averaged radiation intensity is equal to the total power radiated divided by 4π.

Absorption cross section $\sigma_{\mathrm{a}}(\hat{\boldsymbol{k}}, \hat{\boldsymbol{p}}_{\mathrm{e}}, \Gamma)$**.** The absorption cross section for a given polarization and incident direction is the ratio of the absorbed power in the antenna to the incident power flow density when subject to a plane-wave excitation. For a perfectly matched antenna, the absorption cross section coincides with the partial effective area.

Scattering cross section $\sigma_{\mathrm{s}}(\hat{\boldsymbol{k}}, \hat{\boldsymbol{p}}_{\mathrm{e}}, \Gamma)$**.** The scattering cross section for a given polarization and incident direction is the ratio of the scattered power by the antenna to the incident power flow density when subject to a plane-wave excitation.

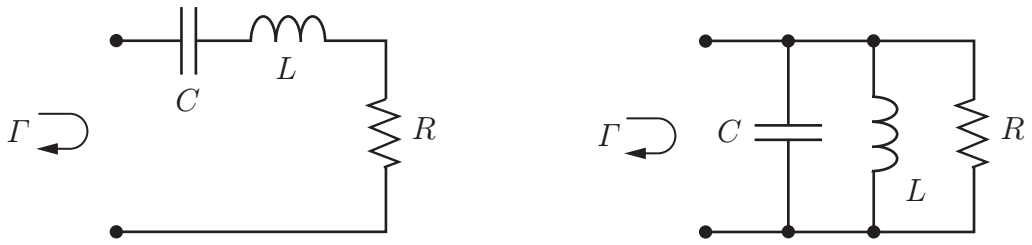

Figure 15: The RCL circuits corresponding to the plus (left figure) and minus (right figure) signs in (F.1).

Extinction cross section $\sigma_{\rm ext}(\hat{\boldsymbol{k}}, \hat{\boldsymbol{p}}_{\rm e}, \Gamma)$. The extinction cross section for a given polarization and incident direction is the sum of the absorbed and scattered power of the antenna to the incident power flow density when subject to a plane-wave excitation, *i.e.*, $\sigma_{\rm ext}(\hat{\boldsymbol{k}}, \hat{\boldsymbol{p}}_{\rm e}, \Gamma) = \sigma_{\rm a}(\hat{\boldsymbol{k}}, \hat{\boldsymbol{p}}_{\rm e}, \Gamma) + \sigma_{\rm s}(\hat{\boldsymbol{k}}, \hat{\boldsymbol{p}}_{\rm e}, \Gamma)$.

Absorption efficiency[5] **$\eta(\hat{\boldsymbol{k}}, \hat{\boldsymbol{p}}, \Gamma)$.** The absorption efficiency of an antenna for a given polarization and incident direction is the ratio of the absorbed power to the total absorbed and scattered power when subject to a plane-wave excitation, *i.e.*, $\eta(\hat{\boldsymbol{k}}, \hat{\boldsymbol{p}}_{\rm e}, \Gamma) = \sigma_{\rm a}(\hat{\boldsymbol{k}}, \hat{\boldsymbol{p}}_{\rm e}, \Gamma)/\sigma_{\rm ext}(\hat{\boldsymbol{k}}, \hat{\boldsymbol{p}}_{\rm e}, \Gamma)$.

Quality factor Q. The quality factor of a resonant antenna is the ratio of 2π times the energy stored in the fields excited by the antenna to the energy radiated and dissipated per cycle. For electrically small antennas, it is equal to one-half the magnitude of the ratio of the incremental change in impedance to the corresponding incremental change in frequency at resonance, divided by the ratio of the antenna resistance to the resonant frequency.

Appendix F Q-factor and bandwidth

The quality factor, or Q-factor, is often used to estimate the bandwidth of an antenna. It is defined as the ratio of the energy stored in the reactive field to the radiated energy, *i.e.*, $Q = 2\omega \max(W_{\rm m}, W_{\rm e})/P$, see Appendix E and Refs. 6 and 25. Here, $W_{\rm e}$ and $W_{\rm m}$ denote the stored electric and magnetic energies, respectively, P is the dissipated power, and $\omega = kc_0$ the angular frequency. At the resonance, $k = k_0$, there are equal amounts of stored electric and magnetic energy, *i.e.*, $W_{\rm e} = W_{\rm m}$.

For many applications it is sufficient to model the antenna as a simple RCL resonance circuit around the resonance frequency. The reflection coefficient Γ of the antenna is then given by

$$\Gamma = \frac{Z(k) - R}{Z(k) + R} = \pm \frac{1 - (k/k_0)^2}{1 - (k/k_0)^2 - 2{\rm i}k/(k_0 Q)} \tag{F.1}$$

[5]This term is not defined in Ref. 13; the present definition is instead based on Ref. 2.

where Z denotes the frequency dependent part of the impedance, and the plus and minus signs in (F.1) correspond to the series and parallel circuits in Fig. 15, respectively. The reflection coefficient Γ is holomorphic in the upper half plane $\mathrm{Im}\,\omega > 0$ and characterized by the poles

$$k = \pm k_0\sqrt{1 - Q^{-2}} - \mathrm{i}k_0/Q, \tag{F.2}$$

which are symmetrically distributed with respect to the imaginary axis.

The bandwidth of the resonances in (F.2) depends on the threshold level of the reflection coefficient. The relative bandwidths of half-power, $|\Gamma|^2 \leq 0.5$, is given by $B \approx 2/Q$. The corresponding losses due to the antenna mismatch are calculated from

$$1 - |\Gamma|^2 = \frac{1}{1 + Q^2(k/k_0 - k_0/k)^2/4}. \tag{F.3}$$

The definition of the Q-factor in terms of the quotient between stored and radiated energies is however not adequate for the present analysis. This is because the decomposition of the total energy into the stored and dissipated parts is a fundamentally difficult task. As noted in Refs. 6 and 25, the Q-factor at the resonance frequency $k = k_0$ can instead be determined by differentiating the reflection coefficient or impedance, *i.e.*,

$$\left|\frac{\partial\Gamma}{\partial k}\right| = \frac{1}{2R}\left|\frac{\partial Z}{\partial k}\right| = \frac{Q}{k_0}, \tag{F.4}$$

where the derivatives in (F.4) are evaluated at $k = k_0$. Relation (F.4) is exact for the single resonance circuit and is also a good approximation for multiple resonance models if Q is sufficiently large. In Sec. (4), a multiple resonance model is considered for the extinction volume ϱ introduced in Appendix A. The multiple resonance model is obtained by superposition of single resonance terms with poles of the type (F.2).

Appendix G The depolarizing factors

For the ellipsoids of revolution, *i.e.*, the prolate and oblate spheroids, closed-form expressions of (6.2) exist in terms of the semi-axis ratio $\xi \in [0, 1]$. The result for the prolate spheroid is ($a_2 = a_3$)

$$\begin{cases} L_1(\xi) = \dfrac{\xi^2}{2(1-\xi^2)^{3/2}}\left(\ln\dfrac{1+\sqrt{1-\xi^2}}{1-\sqrt{1-\xi^2}} - 2\sqrt{1-\xi^2}\right) \\ L_2(\xi) = L_3(\xi) = \dfrac{1}{4(1-\xi^2)^{3/2}}\left(2\sqrt{1-\xi^2} - \xi^2\ln\dfrac{1+\sqrt{1-\xi^2}}{1-\sqrt{1-\xi^2}}\right) \end{cases} \tag{G.1}$$

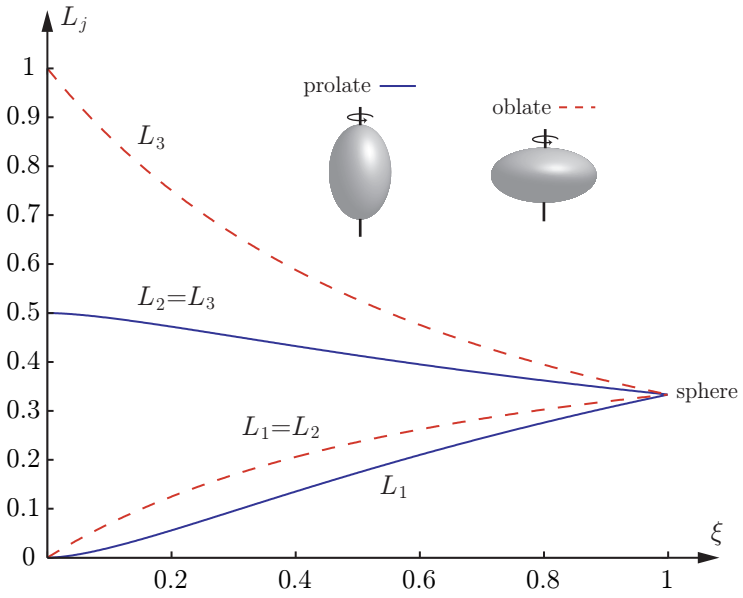

Figure 16: The depolarizing factors for the prolate (solid) and oblate (dashed) spheroids as function of the semi-axis ratio ξ. Note the degeneracy for the sphere.

while for the oblate spheroid ($a_1 = a_2$)

$$\begin{cases} L_1(\xi) = L_2(\xi) = \dfrac{\xi^2}{2(1-\xi^2)}\left(-1 + \dfrac{\arcsin\sqrt{1-\xi^2}}{\xi\sqrt{1-\xi^2}}\right) \\ L_3(\xi) = \dfrac{1}{1-\xi^2}\left(1 - \dfrac{\xi\arcsin\sqrt{1-\xi^2}}{\sqrt{1-\xi^2}}\right) \end{cases} \tag{G.2}$$

The depolarizing factors (G.1) and (G.2) are depicted in Fig. 16. Note that (G.1) and (G.2) differ in indices from the depolarizing factors in Ref. 19 due to the order relation $L_1 \leq L_2 \leq L_3$ assumed in Sec. 6 in this paper.

Introduce the eigenvalues $\gamma_j(\xi) = V(\xi)/L_j(\xi)$ of the high-contrast polarizability dyadic. In terms of the radius a of the smallest circumscribing sphere, the spheroidal volume $V(\xi)$ is given by $\xi^2 4\pi a^3/3$ and $\xi 4\pi a^3/3$ for the prolate and oblate spheroids, respectively. For the analysis in Sec. 6, the limit of $\gamma_j(\xi)$ as $\xi \to 0$ is particular interesting, corresponding to the circular needle for the prolate spheroid and the circular disk for the oblate spheroid. The result for the circular needle reads

$$\begin{cases} \gamma_1(\xi) = \dfrac{4\pi a^3}{3}\dfrac{1}{\ln 2/\xi - 1} + \mathcal{O}(\xi^2) \\ \gamma_2(\xi) = \gamma_3(\xi) = \mathcal{O}(\xi^2) \end{cases} \quad \text{as } \xi \to 0 \tag{G.3}$$

while for the circular disk,

$$\begin{cases} \gamma_1(\xi) = \gamma_2(\xi) = \dfrac{16a^3}{3} + \mathcal{O}(\xi) \\ \gamma_3(\xi) = \mathcal{O}(\xi) \end{cases} \quad \text{as } \xi \to 0 \tag{G.4}$$

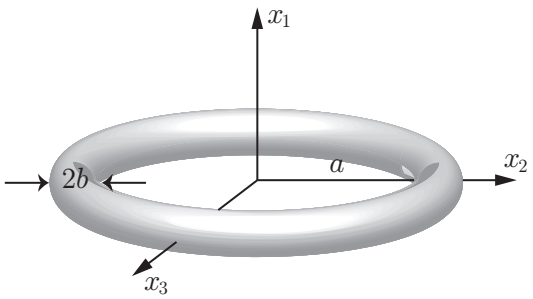

Figure 17: The toroidal ring and the Cartesian coordinate system (x_1, x_2, x_3).

Closed-form expressions of (6.2) can also be evaluated for the elliptic needle and disk in terms of the complete elliptic integrals of the first and second kind, see Ref. 19.

Appendix H The toroidal ring

The general solution to Laplace's equation for the electrostatic potential ψ in toroidal coordinates[6] is, see Ref. 15,

$$\psi(u,v,\phi) = \sqrt{\cosh v - \cos u} \sum_{n,m=0}^{\infty} (a_m \cos m\phi + b_m \sin m\phi) \cdot (c_m \cos nu + d_m \sin nu) \left(A_{mn} \mathrm{P}^m_{n-\frac{1}{2}}(\cosh v) + B_{mn} \mathrm{Q}^m_{n-\frac{1}{2}}(\cosh v) \right),$$

where $\mathrm{P}^m_{n-1/2}$ and $\mathrm{Q}^m_{n-1/2}$ are the ring functions of the first and second kinds, respectively, see Ref. 1. The toroidal ring of axial radius a and cross section radius b is given by the surface $v = v_0$, see Fig. 17. Introduce the semi-axis ratio $\xi \in [0,1]$ as the quotient $\xi = b/a = 1 \cosh v_0$.

In this appendix, the eigenvalues of the high-contrast polarizability dyadic are derived for the loop antenna in Sec. 8.2 of vanishing thickness. Due to rotational symmetry in the x_1x_2-plane, the analysis is reduced to two exterior boundary value problems defined by the region $v \in [0, v_0]$ and $u, \phi \in [0, 2\pi)$. Due to the singular behavior of $\mathrm{Q}^m_{n-1/2}(\cosh v)$ as $v \to 0$ it is required that $B_{mn} = 0$. In addition, the electrostatic potential must vanish at infinity, *i.e.*, $\psi(u,v,\phi) \to 0$ when $u, v \to 0$ simultaneously. On the surface of the toroidal ring the two different boundary conditions of interest are, $\psi(u, v_0, \phi) = x_1$ and $\psi(u, v_0, \phi) = x_3$, see Appendix B.

[6]The toroidal coordinate system (u,v,ϕ) is defined in terms of the Cartesian coordinates (x_1, x_2, x_3) as

$$x_1 = \frac{\zeta \sinh v \cos\phi}{\cosh v - \cos u}, \qquad x_2 = \frac{\zeta \sinh v \sin\phi}{\cosh v - \cos u}, \qquad x_2 = \frac{\zeta \sin u}{\cosh v - \cos u},$$

where $u, \phi \in [0, 2\pi)$ and $v \in [0, \infty)$. The toroidal ring of axial radius a and cross section radius b is described by the surface $v = v_0$, where $a = \zeta \coth v_0$ and $b = \zeta / \sinh v_0$. Note that the present notation (u,v,ϕ) differs from (η, μ, ϕ) in Ref. 15.

The following representations of the Cartesian coordinates in terms of $\mathrm{Q}^m_{n-1/2}$ are proved to be useful:

$$\begin{cases} x_1 = -\dfrac{\zeta\sqrt{8}\cos\phi}{\pi}\sqrt{\cosh v_0 - \cos u}\displaystyle\sum_{n=0}^{\infty}\varepsilon_n \mathrm{Q}^1_{n-\frac{1}{2}}(\cosh v_0)\cos nu \\ x_3 = \dfrac{\zeta\sqrt{8}}{\pi}\sqrt{\cosh v_0 - \cos u}\displaystyle\sum_{n=1}^{\infty} n\mathrm{Q}_{n-\frac{1}{2}}(\cosh v_0)\sin nu \end{cases} \tag{H.1}$$

Two different boundary value problems are associated with the loop antenna in Sec. 8.2 depending on whether the magnetic polarization $\hat{\boldsymbol{p}}_{\mathrm{m}}$ is parallel or orthogonal to the x_3-axis. The solution of these boundary value problems are then closely related to the components of the electric polarizability dyadic. Only the case when the thickness of the toroidal ring vanishes, *i.e.*, when $\xi \to 0$ or equivalently $v_0 \to \infty$, is treated here.

H.1 Magnetic polarization perpendicular to the x_3-axis

A magnetic polarization $\hat{\boldsymbol{p}}_{\mathrm{m}}$ perpendicular to the x_3-axis is via the plane-wave condition $\hat{\boldsymbol{k}} = \hat{\boldsymbol{p}}_{\mathrm{e}} \times \hat{\boldsymbol{p}}_{\mathrm{m}}$ equivalent to the electric polarization $\hat{\boldsymbol{p}}_{\mathrm{e}}$ parallel with the x_3-axis. A straightforward calculation to this problem can be proved to yield

$$\psi(u,v,\phi) = \frac{\zeta\sqrt{8}}{\pi}\sqrt{\cosh v - \cos u}\sum_{n=1}^{\infty} n\frac{\mathrm{Q}_{n-\frac{1}{2}}(\cosh v_0)}{\mathrm{P}_{n-\frac{1}{2}}(\cosh v_0)}\mathrm{P}_{n-\frac{1}{2}}(\cosh v)\sin nu.$$

In terms of the normal derivative $\partial\psi/\partial\nu$ evaluated at $v = v_0$, the third eigenvalue of $\boldsymbol{\gamma}_\infty$ is given by

$$\gamma_3 = 2\pi\int_0^{2\pi} x_3\frac{\partial\psi(u,v_0,\phi)}{\partial\nu}\frac{\zeta^2\sinh v_0}{(\cosh v_0 - \cos u)^2}\,\mathrm{d}u \tag{H.2}$$

By insertion of (H.1) into (H.2), the asymptotic behavior of γ_3 in the limit $\xi \to 0$, or equivalently $v_0 \to \infty$, can be proved to be ($\zeta \to a$ as $v_0 \to \infty$)

$$\gamma_3 = \mathcal{O}(\xi^2) \quad \text{as } \xi \to 0. \tag{H.3}$$

Hence, the third eigenvalue γ_3 of the high-contrast polarizability dyadic vanishes as the thickness of the toroidal ring approaches zero.

H.2 Magnetic polarization parallel with the x_3-axis

The solution to the boundary value problem with the magnetic polarization $\hat{\boldsymbol{p}}_{\mathrm{m}}$ parallel with the x_3-axis, *i.e.*, $\hat{\boldsymbol{p}}_{\mathrm{e}}$ perpendicular to the x_1-axis, is

$$\psi(u,v,\phi) = -\frac{\zeta\sqrt{8}\cos\phi}{\pi}\sqrt{\cosh v - \cos u}\sum_{n=0}^{\infty}\varepsilon_n\frac{\mathrm{Q}^1_{n-\frac{1}{2}}(\cosh v_0)}{\mathrm{P}^1_{n-\frac{1}{2}}(\cosh v_0)}\mathrm{P}^1_{n-\frac{1}{2}}(\cosh v)\cos nu,$$

where $\varepsilon_n = 2 - \delta_{n0}$ is the Neumann factor. In terms of the normal derivative $\partial\psi/\partial\nu$ evaluated at $v = v_0$, the first and second eigenvalues of $\boldsymbol{\gamma}_\infty$ are

$$\gamma_1 = \gamma_2 = \int_0^{2\pi} \int_0^{2\pi} x_1 \frac{\partial\psi(u, v_0, \phi)}{\partial\nu} \frac{\zeta^2 \sinh v_0}{(\cosh v_0 - \cos u)^2} \, \mathrm{d}\phi \, \mathrm{d}u, \tag{H.4}$$

where x_1 as function of u and ϕ is given by (H.1). The asymptotic behavior of (H.4) as $\xi \to 0$, or equivalently $v_0 \to \infty$, can be proved to be ($\zeta \to a$ as $v_0 \to \infty$)

$$\gamma_1 = \gamma_2 = \frac{2\pi^2 a^3}{\ln 2/\xi - 1} + \mathcal{O}(\xi^2) \quad \text{as } \xi \to 0. \tag{H.5}$$

Note that (H.5) vanishes slower than (H.3) as $\xi \to 0$ due to the logarithmic singularity.

References

[1] M. Abramowitz and I. A. Stegun, editors. *Handbook of Mathematical Functions*. Applied Mathematics Series No. 55. National Bureau of Standards, Washington D.C., 1970.

[2] J. B. Andersen and A. Frandsen. Absorption efficiency of receiving antennas. *IEEE Trans. Antennas Propagat.*, **53**(9), 2843–2849, 2005.

[3] L. J. Chu. Physical limitations of omni-directional antennas. *Appl. Phys.*, **19**, 1163–1175, 1948.

[4] R. S. Elliott. *Antenna Theory and Design*. IEEE Press, New York, 2003. Revised edition.

[5] R. M. Fano. Theoretical limitations on the broadband matching of arbitrary impedances. *Journal of the Franklin Institute*, **249**(1,2), 57–83 and 139–154, 1950.

[6] M. Gustafsson and S. Nordebo. Bandwidth, Q-factor, and resonance models of antennas. *Progress in Electromagnetics Research*, **62**, 1–20, 2006.

[7] M. Gustafsson, C. Sohl, and G. Kristensson. Physical limitations on antennas of arbitrary shape. *Proc. R. Soc. A*, **463**, 2007. doi:1098/rspa.2007.1893.

[8] M. Gustafsson. On the non-uniqueness of the electromagnetic instantaneous response. *J. Phys. A: Math. Gen.*, **36**, 1743–1758, 2003.

[9] M. Gustafsson and S. Nordebo. Characterization of MIMO antennas using spherical vector waves. *IEEE Trans. Antennas Propagat.*, **54**(9), 2679–2682, 2006.

[10] E. Hallén. *Theoretical investigations into the transmitting and receiving qualities of antennae*, volume 11, No. 4 of *Nova acta Regiae Societatis Scientarium Upsaliensis IV*. Almqvist & Wiksell, Stockholm, 1938. ISSN 0029-5000; Ser. 4, 11:4.

[11] M. Hamermesh. *Group theory and its application to physical problems*. Dover Publications, New York, 1989.

[12] R. C. Hansen. *Electrically small, superdirective, and superconductive antennas*. John Wiley & Sons, New Jersey, 2006.

[13] IEEE Standard Definitions of Terms for Antennas, 1993. IEEE Std 145-1993. ISBN 1-55937-317-2.

[14] R. E. Kleinman and T. B. A. Senior. Rayleigh scattering. In V. V. Varadan and V. K. Varadan, editors, *Low and high frequency asymptotics*, volume 2 of *Acoustic, Electromagnetic and Elastic Wave Scattering*, chapter 1, pages 1–70. Elsevier Science Publishers, Amsterdam, 1986.

[15] P. M. Morse and H. Feshbach. *Methods of Theoretical Physics*, volume 2. McGraw-Hill, New York, 1953.

[16] R. G. Newton. *Scattering Theory of Waves and Particles*. Springer-Verlag, New York, 1982.

[17] H. M. Nussenzveig. *Causality and dispersion relations*. Academic Press, London, 1972.

[18] S. Silver. *Microwave Antenna Theory and Design*, volume 12 of *Radiation Laboratory Series*. McGraw-Hill, New York, 1949.

[19] C. Sohl, M. Gustafsson, and G. Kristensson. Physical limitations on broadband scattering by heterogeneous obstacles. Accepted for publication in J. Phys. A: Math. Theor., 2007.

[20] C. Sohl, M. Gustafsson, and G. Kristensson. Physical limitations on metamaterials: Restrictions on scattering and absorption over a frequency interval. Technical Report LUTEDX/(TEAT-7154)/1–10/(2007), Lund University, Department of Electrical and Information Technology, P.O. Box 118, S-221 00 Lund, Sweden, 2007. http://www.eit.lth.se.

[21] W. L. Stutzman and G. A. Thiele. *Antenna Theory and Design*. John Wiley & Sons, New York, second edition, 1998.

[22] J. R. Taylor. *Scattering theory: the quantum theory of nonrelativistic collisions*. Robert E. Krieger Publishing Company, Malabar, Florida, 1983.

[23] H. van de Hulst. *Light Scattering by Small Particles*. John Wiley & Sons, Inc., New York, 1957.

[24] H. A. Wheeler. Fundamental limitations of small antennas. *Proc. IRE*, **35**(12), 1479–1484, 1947.

[25] A. D. Yaghjian and S. R. Best. Impedance, bandwidth, and Q of antennas. *IEEE Trans. Antennas Propagat.*, **53**(4), 1298–1324, 2005.